LAWRENCE
LIVERMORE
NATIONAL
LABORATORY

LLNL-SM-791163

NEC-5 Validation Manual

G. J Burke

September 24, 2019

Disclaimer

This work performed under the auspices of the U.S. Department of Energy by Lawrence Livermore National Laboratory under Contract DE-AC52-07NA27344.

1. Introduction

The NEC antenna modeling code has been in use since about 1975 in various versions [1, 2]. NEC–5 [3] uses an algorithm new to NEC, solving the electric field integral equation (EFIE) for wires and surfaces using the mixed potential method developed by Rao, Wilton and Glisson [4]. This method is widely used in moment method codes and overcomes many of the limitations of the point-matched algorithm in previous NEC codes. In addition to NEC–5 providing new or more accurate modeling capabilities, comparing results from NEC–5 and 4 can serve as validation of both codes or reveal limitations, since the two codes are mostly independent in their numerical solution methods. If they agree it is pretty likely the result is accurate.

NEC–4 and previous codes solve the EFIE for wires and the magnetic field integral equation (MFIE) for surfaces with point matching of the boundary conditions. The MFIE surface model is limited to closed, perfectly conducting surfaces, and connection of an EFIE wire to a MFIE surface offers limited accuracy at best.

In the mixed-potential method the boundary condition is enforced on approximations of path integrals of the electric field between adjacent element centroids. The integrals of E reduce the order of the singularity of the kernel permitting the EFIE to be used for both surfaces and wires. The integrals of E are approximated in terms of potentials, with the integral of the vector potential $\vec{A}$ approximated using the average of $\vec{A}$ at the centroids and the scalar potential term $\nabla\phi$ approximated from the difference of ϕ at the centroids.

Many people have contributed to the development of the mixed-potential solution method. Throughout its history D. R. Wilton at the University of Houston has been the major coordinator and developer of the techniques. An early code for modeling surfaces was the Patch Code [5], which was followed by the Junction Code [6, 7] allowing connection of wires to surfaces. The method of connecting a wire to a surface comes from the work of Rao [8] and Costa and Harrington [9, 10]. A large effort went into the code EIGER [11], which was essentially a test bed for abstracting ideas and developing object oriented programing methods. The EIGER project resulted in a code that could be extended to higher-order basis functions, curvilinear elements, dielectrics, two-sided surfaces for greater isolation and alternate Green's functions. NEC–5 does not use the developments from EIGER, but starts at the level of wires, patches and junctions with a ground model from the work of Michalski [12, 13].

This validation manual contains results for a number of modeling situations to demonstrate the accuracy or numerical modeling errors of the codes NEC–4 and 5. A separate issue is physical modeling errors which result from simplifying a real antenna in its environment to an idealized form that can be modeled, simplifying parts or neglecting large nearby objects to limit the model size. The significance of physical modeling errors must usually be judged from experience.

Numerical modeling errors result from limitations of the modeling code in enforcing

the boundary conditions, usually related to convergence in the solution. For an accurate numerical model the solution must satisfy Maxwell's equations and the boundary conditions on the fields for the idealized model. Maxwell's equations are pretty much guaranteed, since the Green's function satisfies Maxwell's equations. NEC–4 and 5 use different methods of enforcing the boundary condition on E, so comparison of the results can reveal errors or give good confidence that the results are accurate.

NEC–5 uses a linear current expansion, with triangular and roof-top basis functions and a singular junction basis function to join surface current to a wire current. This linear current expansion may converge somewhat more slowly than the sinusoidal expansion used in previous NEC codes, as shown in this manual for dipoles.

NEC–5 is essentially a complete rewrite of NEC. The input and output have been kept as much as possible the same as in earlier NEC codes. Some differences were unavoidable, since voltage sources in the mixed-potential method are at the ends of segments and on patch edges, while in NEC–4 they are at the segment centers. Patch input is different since patch edges must coincide to be connected. These differences make it somewhat more difficult to build a model file for NEC–5, so graphic assistance is provided, an optional interactive mode while running the code and a separate GUI, NEC5GI [14], to build the model file and view results.

The results in this manual were mostly produced in checking and debugging NEC–5, with comparisons made with NEC–4 for validation. In some cases comparisons are made with classic analytic approximations. Comparisons with experimental data is of course valuable but difficult to come by. Sometimes we receive reports of results supporting NEC, particularly for antennas with ground, but we have not been conscientious in documenting such reports. Also, in experimental results, unless they are done very carefully, the physical modeling errors often exceed the numerical modeling errors which, as seen in results in this manual, are often fairly small.

Sections of this manual cover accuracy of the thin-wire kernel, voltage source models, convergence for a dipole, small loops, surface meshing, wire-surface junctions and wires and loops over ground. Validations for some of these cases have been used in conference papers or the Newsletter of the Applied Computational Electromagnetics Society (ACES) but are probably lost, so this will bring them together. Additional validation results of general interest may be added to this manual as they become available or are contributed by users.

2. Wire Modeling

2.1 The Thin-wire Kernel

A number of approximations are possible in evaluating the kernel for the electric field integral equation for wires. In some early work the current was treated as a filament on the wire axis with the boundary condition enforced on electric field at the wire surface. This convention had the advantage that the current could remain continuous and free of charge singularities at wire bends and steps in radius. However, locating the current on the axis with basis functions continuous to the first derivative in NEC–2 resulted in convergence to the wrong solution at steps in radius. In NEC–4 the current is treated as a filament on the wire surface and the boundary condition is matched on the wire axis. With that change the solution does converge toward the correct behavior at a step in radius. Both of these conventions are called the reduced kernel.

More recently [15, 16] people have used exact thin-wire kernels, where integrals are evaluated over the current on the wire surface and the field is also evaluated on the wire surface. The exact kernel formulations have the advantage that wire segments can have arbitrarily small length relative to their radius. With the reduced kernel the accuracy degrades for segment lengths less than about five times the radius, and the solution for current blows up when the segment length is much shorter than the radius.

A solution with the current on the wire surface and the field matched on the axis can also be exact as an extended boundary condition [17] if the current forms a completely closed surface. However, closing wire ends and the gaps at voltage sources can be difficult. It can be done by assigning additional basis functions and unknowns at the ends and voltage sources [18] or with an approximation of the end-cap current. The approximate end-cap treatment in NEC–4 extended the minimum segment length relative to radius, but it was still limited. All thin wire approximations allow no variation of current around the wire, as would occur when a wire is near another conductor or at a bend.

NEC–5 uses an approximation of the exact kernel as was done in [6]. For demonstration we will consider the scalar potential due to a segment with constant charge density on the z axis, centered at the origin. With the exact kernel the potential at coordinates ρ, z can be written

$$\Phi(\rho, z) = \frac{j}{4\pi\omega\epsilon} \int_{-\Delta/2}^{\Delta/2} \int_{-\pi}^{\pi} \frac{e^{-jkR}}{R}\, d\phi\, dz' \tag{1}$$

where

$$R = \sqrt{\rho^2 + a^2 + (z - z')^2 - 2a\rho\cos\phi} \tag{2}$$

for segment length Δ and radius a and constant unit charge density on the segment. The inner integral over ϕ in (1) is sometimes called the exact kernel.

Following the treatment in [6], the $1/R$ term is removed from a series expansion of the exponential in (1) and integrated accurately, while the reduced kernel approximation is ap-

plied to the reminder. This form, which will be called an extended thin-wire approximation, is

$$\Phi_1(\rho,z) = \frac{j}{4\pi\omega\epsilon}\left(2\pi\int_{-\Delta/2}^{\Delta/2}\frac{e^{-jkR_0}-1}{R_0}\,dz' + \int_{-\Delta/2}^{\Delta/2}\int_{-\pi}^{\pi}\frac{1}{R}\,d\phi\,dz'\right) \tag{3}$$

where

$$R_0 = \sqrt{\rho^2+a^2+(z-z')^2}$$

is R evaluated for $\phi = \pi/2$. The reduced kernel evaluation involves the single integral

$$\Phi_0(\rho,z) = \frac{j}{2\omega\epsilon}\int_{-\Delta/2}^{\Delta/2}\frac{e^{-jkR_0}}{R_0}\,dz'. \tag{4}$$

The accuracy of the reduced and extended kernels relative to the exact kernel were compared using numerical evaluation of the integrals in the program Mathematica [19]. The NIntegrate function in Mathematica can numerically evaluate integrals including integrable singularities, so can be used to evaluate the integrals in (1), (3) and (4) including when the evaluation point is on the wire surface. Interpretation of the error is somewhat problematic, due to the choices in locating the evaluation points. As an extended boundary condition, evaluation points on the axis may yield a solution as accurate as with evaluation on the surface, so differences in potential evaluations for individual segments or matrix elements may not always translate to errors in the solution when all of the matrix elements are taken together. However, the comparison still provides an indication of the limitations of the approximations.

The errors of the extended and reduced kernels over a range of segment lengths Δ and radius a are plotted in Fig. 1 for the self-term evaluation at the midpoint of the segment. The extended kernel was evaluated at the wire surface, $\Phi_1(a,0)$. The reduced kernel was evaluated at the center of the segment, $\Phi_0(0,0)$, since this is the way it is used, and it resulted in smaller errors relative to the exact kernel than evaluating on the surface at 90 degrees from the current filament. The error in the extended kernel is seen to be nearly independent of Δ and to increase with increasing radius a due to the approximate evaluation of the first integral in (3) containing the phase information. The error in the reduced kernel depends on the thickness ratio, and is poor when Δ/a is on the order of 1 or less.

Similar plots are included in Appendix A for ρ equal to 3, 10 and 100 times a and for increasing z. With increasing ρ the extended kernel accuracy remains limited by the phase error. For the reduced kernel the error related to Δ/a decreases with increasing ρ, and the phase error becomes the limiting factor at large a/λ. With increasing z the extended kernel is limited only by the phase error which decreases with increasing z. For the reduced kernel both the error related to Δ/a and the phase error decrease with increasing z.

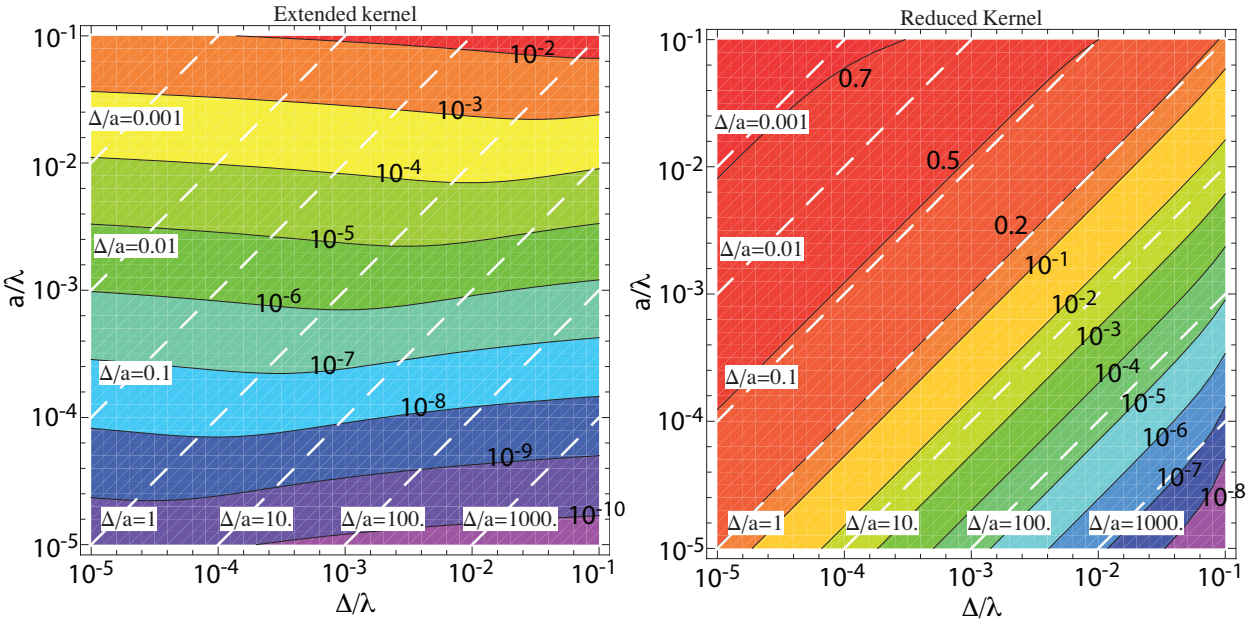

Fig. 2.1.1 Errors in the extended and reduced kernels relative to the exact kernel for the evaluation point at the center of the segment (self-term) with $\rho = a$ for the extended kernel, $\rho = 0$ for the reduced kernel.

In the NEC-5 code the second integral in (3) is evaluated first over z' in terms of log functions. The log function result can be written so that the part that becomes singular as the evaluation point approaches the surface can be integrated exactly. The remaining smoothly varying terms are integrated with a low order Gauss-Legendre rule. Singularity extraction is needed only when the evaluation point approaches near one of the segment ends. The numerical errors in this evaluation appear not to be significant compared to the approximations in the kernel.

Results Testing the Thin-wire Kernel

The effectiveness of the extended kernel can be demonstrated by modeling a dipole antenna with extended and reduced kernels. Solutions for current on a dipole with length $L = 0.5\lambda$ and radius $a = 0.01\lambda$ (thickness parameter $\Omega = 2\log(L/a) = 7.8$) using the reduced kernel in NEC–5 are shown in Fig. 2. The current blows up to large values near the source and ends. Instability also occurs with 80 and 160 segments but is covered in the plot. Solutions obtained with the NEC–5 extended kernel are plotted in Fig. 7 and show no instability up to 640 segments.

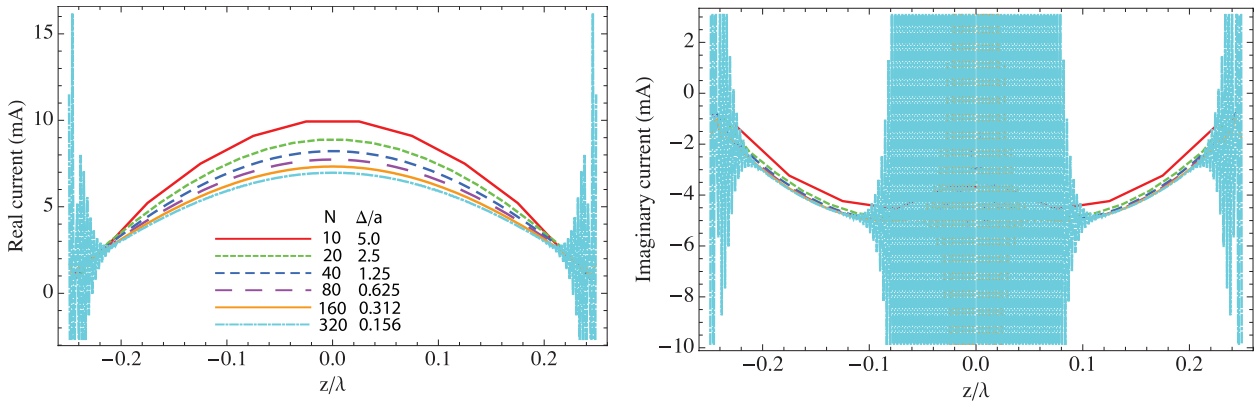

Fig. 2.1.2 Current on a dipole with length $L = 0.5\lambda$, radius $a = 0.01\lambda$ modeled with N segments and segment length $\Delta = L/N$ with the reduced kernel in NEC–5.

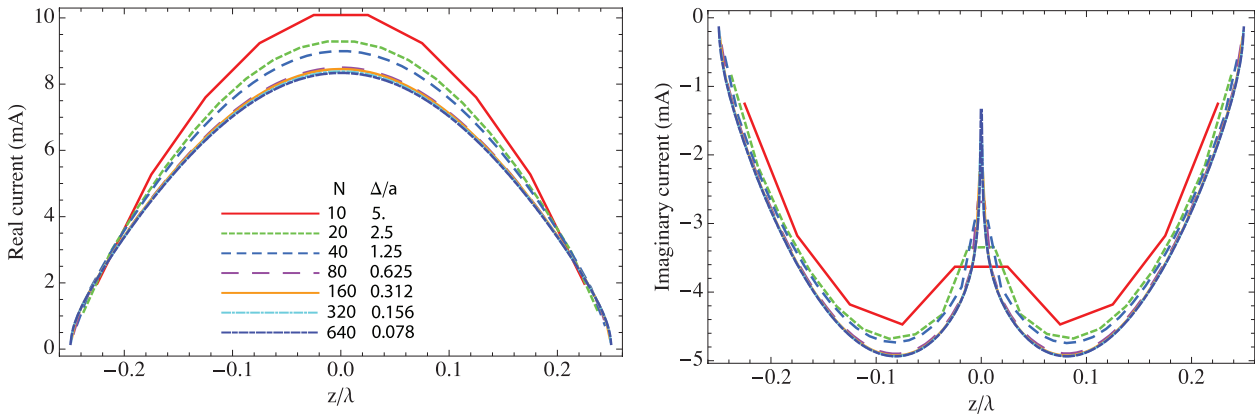

Fig. 2.1.3 Current on the same dipole as Fig. 2 modeled with the extended kernel in NEC–5.

The input admittance computed for this dipole with the NEC–5 extended and reduced kernels and the NEC–4 reduced kernel are shown in Fig. 4 The reduced kernel results blow up to large values for Δ/a less than about 0.16, while the extended kernel converges smoothly to $\Delta/a = 0.01$ with 5000 segments on the dipole. The linear increase in B_{in} is due to the increasing effective shunt capacitance as the source gap becomes narrower, and is normally seen in such solutions. It could be eliminated by dividing the source voltage between multiple segments to keep the width of the source gap constant. In a plot of impedance this changing B_{in} would affect both real and imaginary parts, so that the result would appear not to converge. The relatively large difference between NEC–4 and NEC–5 for large Δ/a is due to convergence, since the 0.5λ dipole is on the steep slope of the admittance curve resonance.

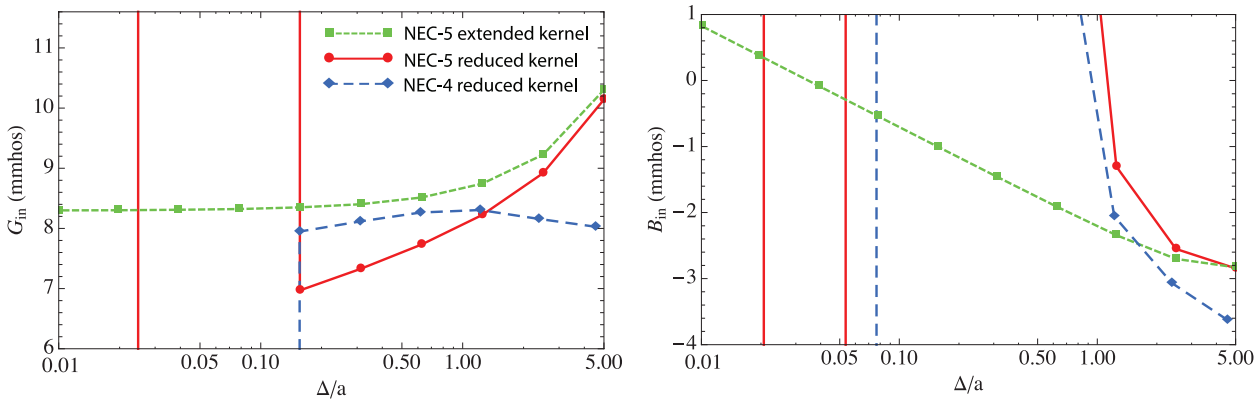

Fig. 2.1.4 Input admittance of a dipole with length $L = 0.5\lambda$ and radius $a = 0.01\lambda$ for varying segment length $\Delta = L/N$.

The computed input admittance of a square loop antenna with side length 0.1λ and wire radius 0.01λ is shown in Fig. 5. Again, the NEC–4 and NEC–5 results using the reduced kernel fail for Δ/a less than about 1, while the NEC–5 extended kernel result converges smoothly. For small segment lengths there are many segments buried within other segments at the corners.

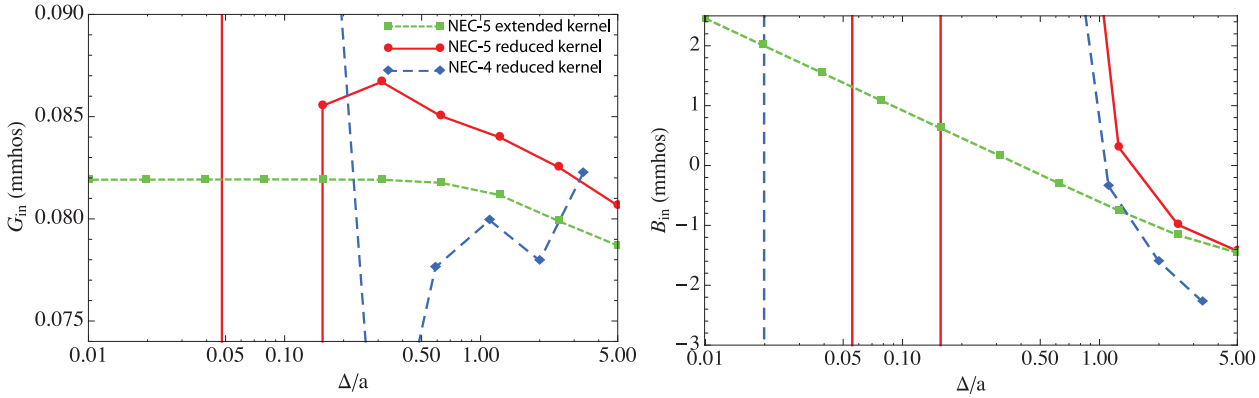

Fig. 2.1.5 Input admittance of a square loop antenna with side length 0.1λ, radius $a = 0.01\lambda$ for varying segment length Δ.

A test for modeling closely spaced wires is provided by a two wire transmission line. Transmission lines are usually modeled with parallel wires connected with short wires at the ends for the source and termination. This model would combine wires that may be closely spaced compared to their radius and segments with small Δ/a at the terminations. To separate closely spaced wires from the small Δ/a problem, two parallel wires were modeled with lengths of 10 m and radius 0.001 m driven with voltage sources of 1 volt and -1 volt at their centers. This model can be cut in half with a PEC plane to have a single open-circuited transmission line with a net 1 volt source.

The input admittance of an ideal open circuited line of length l at frequency f is

$$Y_{\text{in}} = (j/Z_0)\tan(2\pi f l/c)$$

where c the velocity of light and Z_0 the characteristic impedance. Since the line was modeled around 5λ length (5 m at 299.8 MHz) the slope of Y_{in} with frequency was used to determine Z_0. The derivative of Y_{in} is

$$\frac{dY_{\text{in}}}{df} = \frac{2\pi jl}{Z_0 c} \sec^2\left(\frac{2\pi fl}{c}\right).$$

When the line length is a multiple of a half wavelength the characteristic impedance can be estimated as

$$Z_0 = \frac{2\pi l}{c} / (dB_{\text{in}}/df)$$

where B_{in} is the imaginary part of Y_{in} and the derivative is approximated from numerical values about 299.8 MHz.

Results for Z_0 from solutions with NEC–5 extended and reduced kernels and NEC–4 reduced kernel are shown in Fig. 6 and compared with the characteristic impedance of an ideal parallel-wire transmission line

$$Z_0 = \frac{\eta_0}{\pi} \cosh^{-1}\left(\frac{s}{d}\right).$$

Results from the NEC–5 extended and reduced kernels essentially coincide, and the NEC–4 result is close. None of the thin-wire kernel results track the ideal characteristic impedance for s/d less than about 2. The transmission line was also modeled in NEC–5 with cylindrical conductors of rectangular patches, with 400 patches in the 10 m length and 8 patches around the conductor. The patch result in Fig. 6 does track the steeper slope of Z_0 down to $s/d = 1.1$.

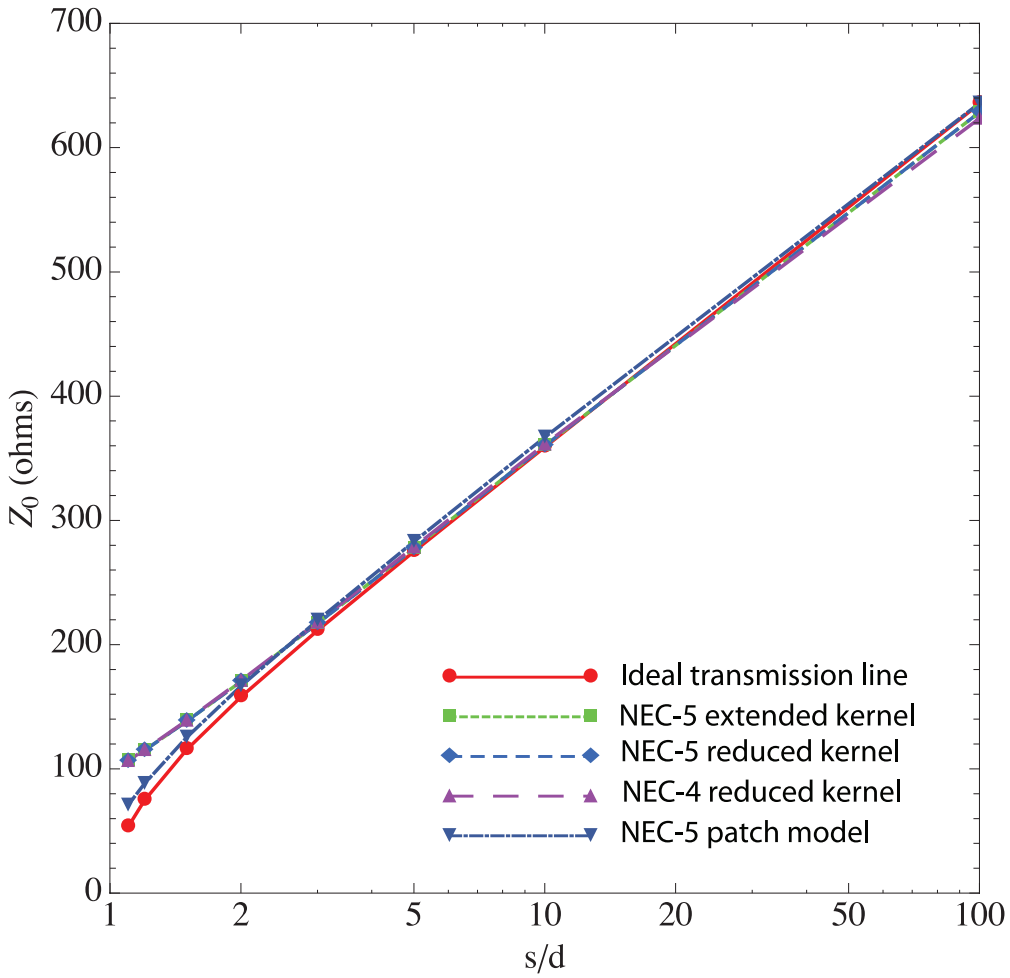

Fig. 2.1.6 Characteristic impedance of a two-wire transmission line for wire separation s and diameter d determined by processing the computed input impedance of an open circuited line modeled with reduced and extended thin-wire kernels and a patch model.

The wire radius in this transmission line is about 0.001λ, so from Fig. 1 the relative error in the self term should be around 10^{-6} with the extended kernel and 10^{-3} with the reduced kernel. For closely spaced adjacent wires the reduced kernel error would be considerably larger. So more accuracy in the extended thin-wire kernel probably would not change the result. The current on a section of one conductor of the patch transmission line model is shown in Fig. 7 for varying wire separation. The current is seen to concentrate between the conductors as the wires become close together, so that the separation of currents is less than the separation of the conductor centers.

It has also been observed with a code using a 2D periodic Green's function that the shielding by a screen of parallel wires reaches a maximum when the wire spacing is $2\pi a$ for wire radius a with either the reduced or essentially exact thin-wire kernel. So the "equal area rule" should still hold with the NEC–5 extended kernel. Of course, there should not be much need for wire grid modeling with the patch model.

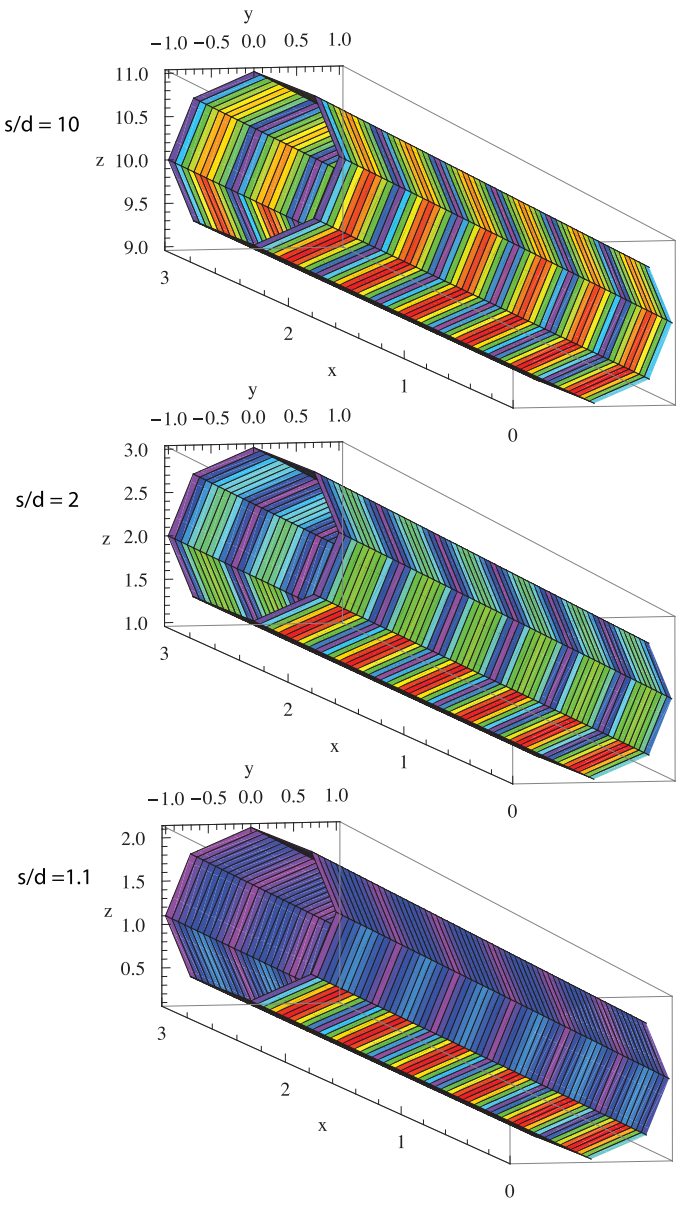

Fig. 2.1.7 Current on the upper conductor of a section of two-wire transmission line modeled as a cylinder with rectangular patches as the separation s is varied for wire diameter $d = 0.002\lambda$. Transverse dimensions have been multiplied by 1000.

2.2 Voltage Source Models

Accurate modeling of voltage sources is critical in modeling antennas to get accurate input impedances and antenna gains. The voltage source models in the point-matched NEC–4 solution and the mixed-potential NEC–5 solution differ substantially, so different modeling rules will apply. In NEC–4 the source is located on a segment, and the voltage drop is approximately spread over the width of the segment. In NEC–5 the voltage source is located at the end of a wire segment or at the edge of a patch. Current sources in NEC-5 are voltage sources with the voltage determined to produce the desired current, so the same modeling rules apply. Also, lumped loads and networks use the voltage source model. The results in this section demonstrate some effects of modeling changes on voltage source accuracy and the effective width of the source.

In NEC–4 a voltage source with strength V_s is modeled by setting the electric field value at the center match point on a segment to $-V_s/\Delta$ for segment length Δ. With a small wire radius and uniform segment lengths in the source region, the electric field has an approximately rectangular distribution over the segment, so that the integral of the field is approximately the voltage V_s. The axial field distribution from a NEC–4 solution for a $\lambda/2$ dipole modeled with 9 segments is shown in Fig. 1. The field distribution over the source segment is somewhat rounded due to the moderate wire radius of 0.001λ. The field away from the source segment is down by nearly two orders of magnitude, and would be smaller with more segments on the dipole. The field shows sharp downward spikes near the match points, although the plot points do not necessarily coincide with match points. Since in NEC–4 the current at segment junctions is continuous to the first derivative, the field is reasonably well behaved at the junctions.

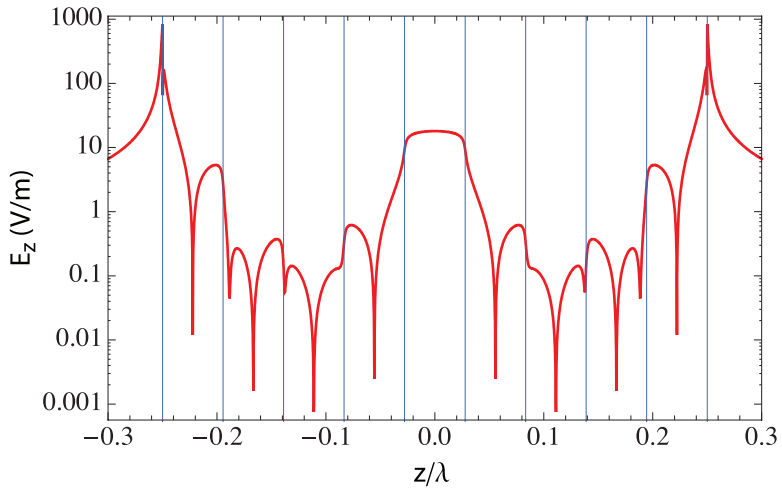

Fig. 2.2.1 Magnitude of electric field along the axis of a dipole antenna with length 0.5λ and radius 0.001λ modeled with 9 segments in NEC–4. Vertical lines mark the ends of segments.

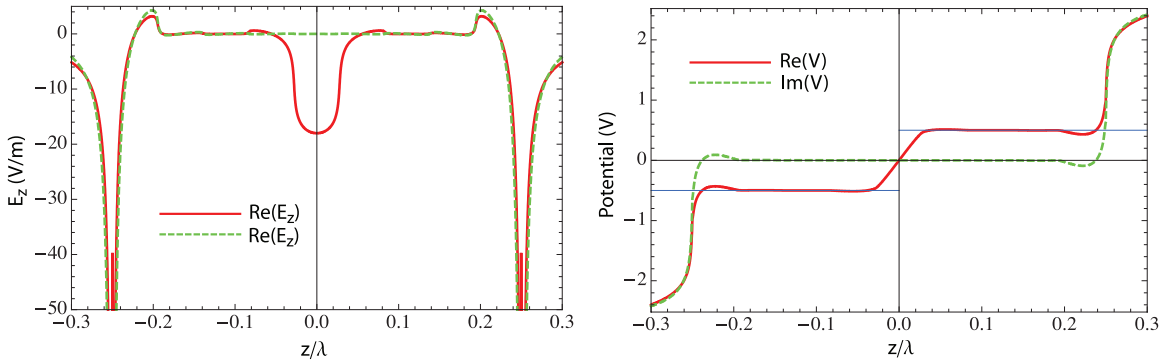

Fig. 2.2.2 Electric field E_z and the potential from integrating $-E_z$ along the axis of a dipole antenna with length 0.5λ and radius 0.001λ modeled with 9 segments in NEC–4.

The real and imaginary parts of E_z from the NEC–4 model of the $\lambda/2$ dipole are plotted in Fig. 2, and also the potential from integrating $-E_z$. The change in potential of 1 volt is seen to take place almost linearly over the source segment.

The field along the $\lambda/2$ dipole modeled with NEC–5 with 8 segments is plotted in Fig. 3. Since NEC–5 uses a piecewise-linear current expansion, the charge density is constant over each segment and discontinuous at the junctions. If an exact kernel were used in calculating the field there would be delta functions of E at the junctions. While NEC–5 uses an extended kernel for the potentials in the solution for current, it uses the reduced kernel for the fields, so the spikes between segments are spread over a width on the order of the wire radius. There are no match points in the mixed-potential solution, so no points where the error in field must be very small. The potential from integrating E_z in Fig. 3 is seen to oscillate around the correct values. While the field and potential plots in Fig. 3 do not look so nice, the mixed-potential solution for antenna impedance and fields away from the antenna can be quite accurate, and in many case as good or better than with NEC–4. Plots of the field and potential when the dipole is modeled with 16 and 32 segments in NEC–5 are shown in Fig. 4 and 5. The field is seen to converge toward the correct values.

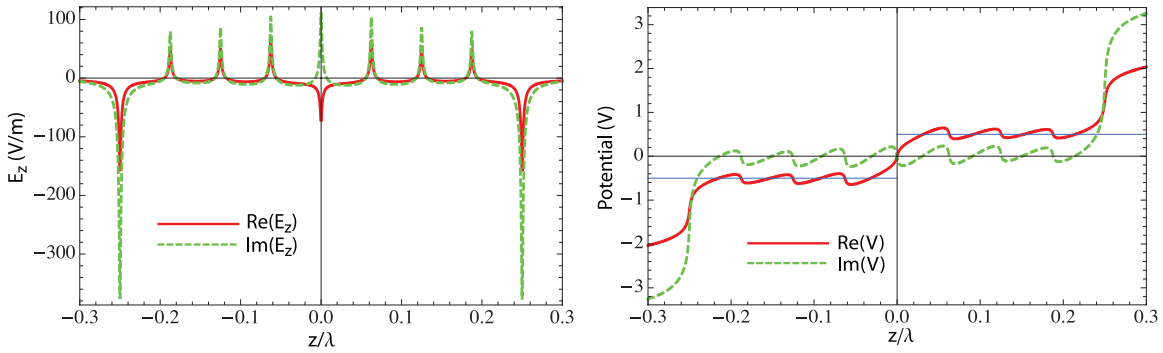

Fig. 2.2.3 Electric field E_z and the potential from integrating $-E_z$ along the axis of a dipole antenna with length 0.5λ and radius 0.001λ modeled with 8 segments in NEC–5.

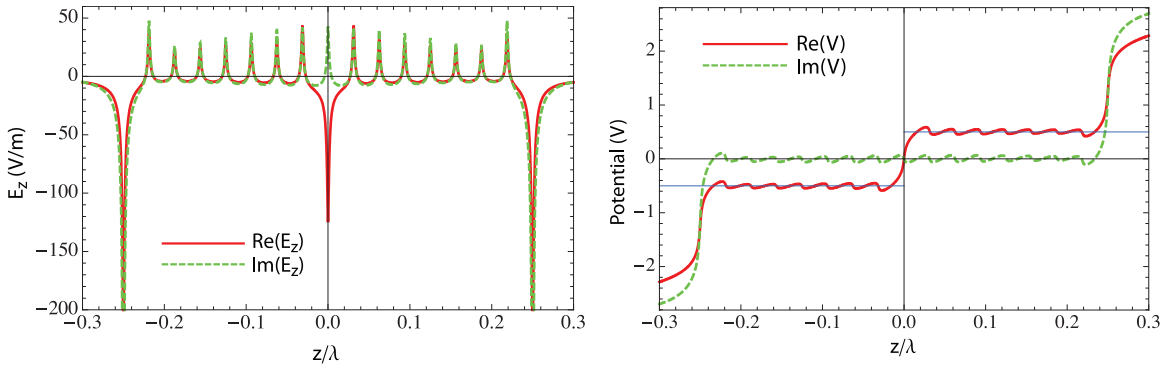

Fig. 2.2.4 Electric field E_z and the potential from integrating $-E_z$ along the axis of a dipole antenna with length 0.5λ and radius 0.001λ modeled with 16 segments in NEC–5.

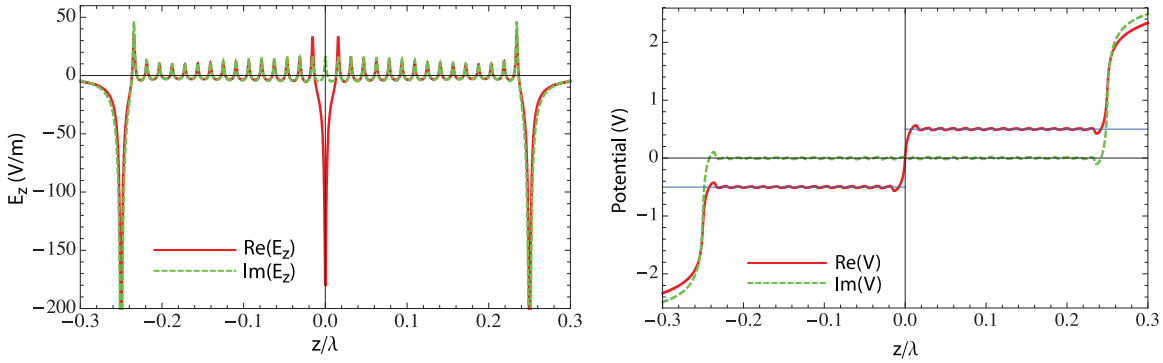

Fig. 2.2.5 Electric field E_z and the potential from integrating $-E_z$ along the axis of a dipole antenna with length 0.5λ and radius 0.001λ modeled with 32 segments in NEC–5.

Since the NEC–4 source is located on a segment, a center fed dipole is usually modeled with an odd number of segments. In NEC–5 the dipole would be modeled with an even number of segments to have a junction at the center. This difference is a barrier to complete compatibility between NEC–4 and 5 models. With NEC–4 the dipole can be modeled with an even number of segments and the center two segments each excited with half the total voltage. The source width is then doubled. Alternately, a dipole can be modeled in NEC–5 with an odd number of segments and the voltage source split between the ends of the center segment. The potential distributions from splitting the source in NEC–5 are shown in Fig. 6 for dipoles with 9 and 17 segments. The split NEC-5 source has a somewhat wider distribution than the NEC–4 source on a single segment, but it provides a reasonable model for a source on a segment. An option could be added to NEC–5 to split all voltage sources, loads and network connections for compatibility with NEC–4 models, but that option is not in the present code.

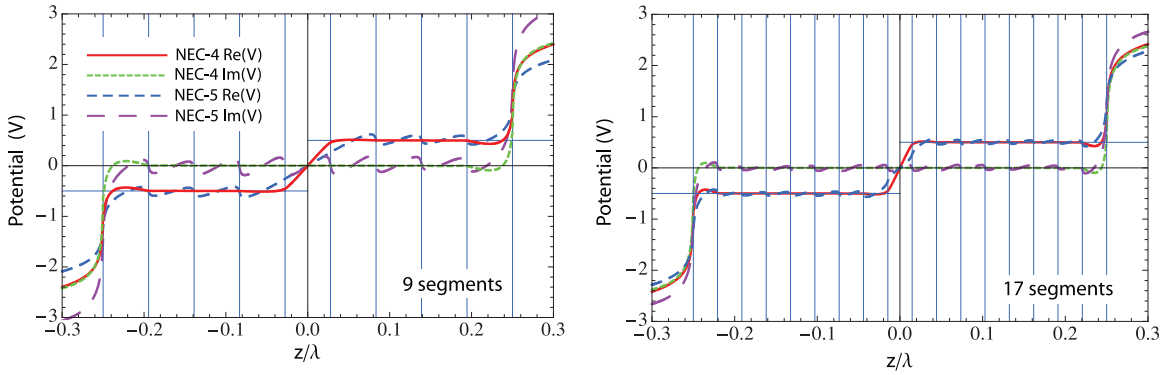

Fig. 2.2.6 Potential along the $\lambda/2$ dipole antenna with radius 0.001λ modeled with 9 and 17 segments. In NEC–4 the 1 volt source was on the center segment and in NEC–5 it was split between the ends of the center segment.

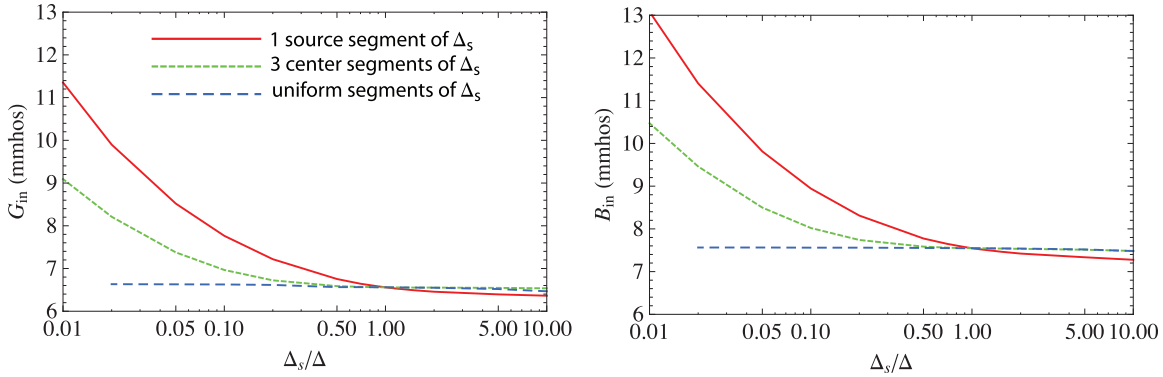

Fig. 2.2.7 Input admittance of a 0.475λ dipole with radius $10^{-6}\lambda$ computed with NEC–4. Curve 1: source segment length Δ_s, other segment lengths Δ; Curve 2: center 3 segments Δ_s with source on the center one, other segment lengths Δ; Curve 3: all segments have uniform length approximately Δ_s.

Effects of nonuniform segment lengths

It has always been recommended that a voltage source in NEC–4 should be located on a segment with equal length segments adjacent to it. The result of violating this rule is shown in Fig. 7. For the top curve the length of the center source segment Δ_s is varied with 50 segments with length Δ on either side of the source. The total number of segments is 101. For the second curve in Fig. 7 the center three segments have equal lengths of Δ_s with the source at the center, and the 50 segments on either side have lengths Δ, for a total of 103 segments. For the final curve the dipole is modeled with segments of uniform length Δ_s. Source segments with length differing from the surrounding segments are seen to result in an error in input admittance, with shorter source segments causing larger errors. Having segments of equal length adjacent to the source reduces the error, but it is still a problem.

The power balance, obtained from the "average gain" calculation in NEC–4 and 5 provides another check on solution accuracy. The ratio of radiated power to input power should

be 1.0 when there are no losses involved. The error in power balance is shown in Fig. 8 for varying source segment length. The error is due to error in input resistance, since the integral of radiated power is insensitive to errors in the current. The floor in the error with uniform segmentation is probably due to the accuracy of integrating the radiated power with 2 degree steps in θ.

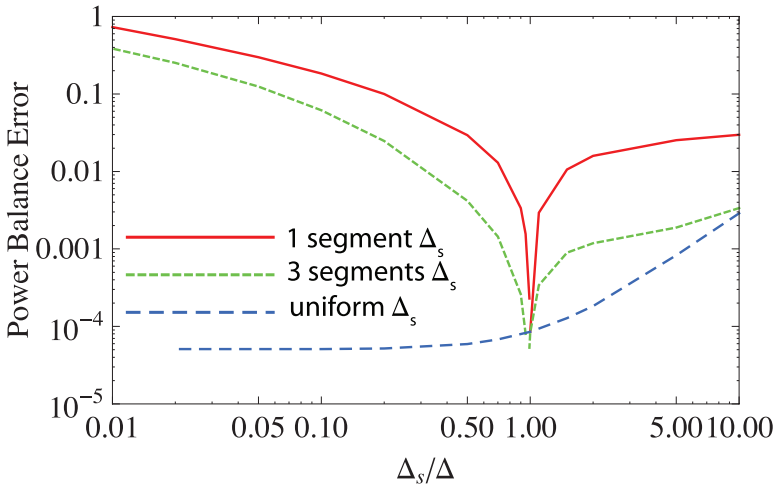

Fig. 2.2.8 Error in the ratio $P_{\rm rad}/P_{\rm in}$ for the NEC–4 dipole models in Fig. 7.

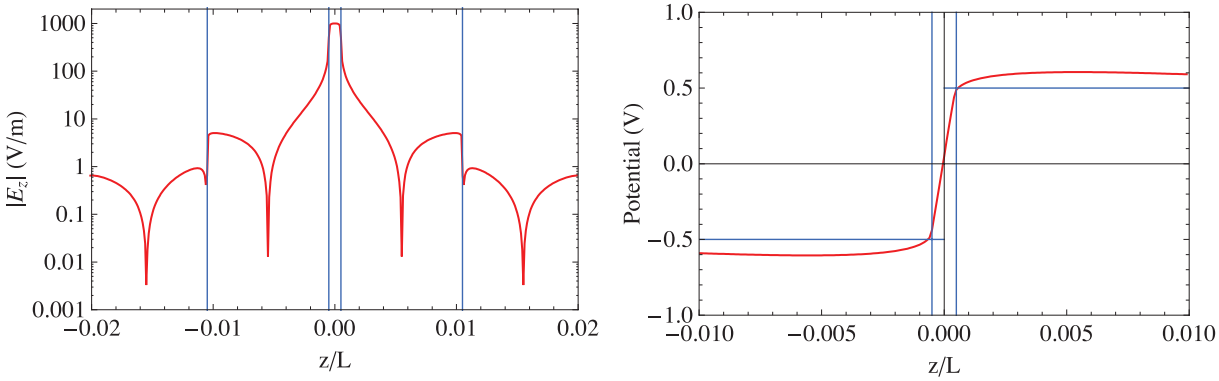

Fig. 2.2.9 Field E_z and integrated potential over the source region of the dipole when the ratio of source segment length to adjacent segment lengths Δ_s/Δ is 0.1 in NEC–4. Vertical lines mark the segment ends.

The electric fields in the source region of the dipole and the potentials from integrating $-E_z$ are shown in Fig. 9 through 11 for Δ_s/Δ of 0.1, 1.0 and 10. With $\Delta_s/\Delta = 0.1$ the source field is mostly localized on the source segment, but large skirts result in an error in the total voltage drop. The error in potential is not as obvious with $\Delta_s/\Delta = 10$, but the drop is somewhat too small.

For the NEC–5 model the two center segments were given lengths Δ_s and the dipole was completed with 50 segments on either side with lengths Δ. The total number of segments was 102. The result for input impedance in Fig. 12 is seen to be very insensitive to Δ_s/Δ.

The power balance error in Fig. 13 also shows low sensitivity to Δ_s/Δ. Plots of the field distribution E_z and potential from integrating $-E_z$ are shown in Fig. 14 through 19. The wire radius has been increased to $10^{-4}\lambda$ to make it easier to sample the field. The effective source width is narrower than the segment length, especially for the wide source segment, but the voltage drop remains correct.

As a final test of the NEC–5 source model half of the dipole was modeled with 50 segments with lengths $\Delta_1 = 0.00475\lambda$ and the number of segments on the other half was varied for segment length Δ_2 with the voltage source at the junction where the segment length changes. The input admittance shown in Fig. 20 is fairly insensitive to the ratio Δ_2/Δ_1. The change that is seen may be due more to convergence with large segments than to error in the source model.

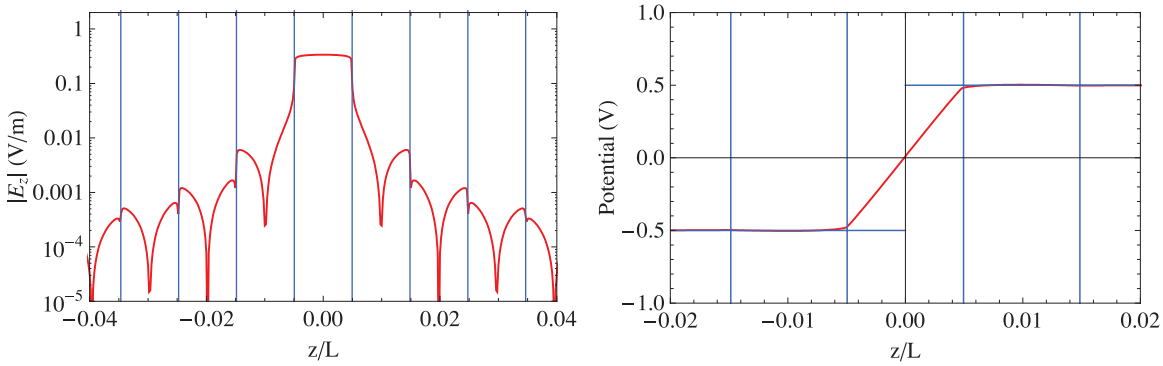

Fig. 2.2.10 Field E_z and integrated potential over the source region of the dipole when the ratio of source segment length to adjacent segment lengths Δ_s/Δ is 1.0 in NEC–4.

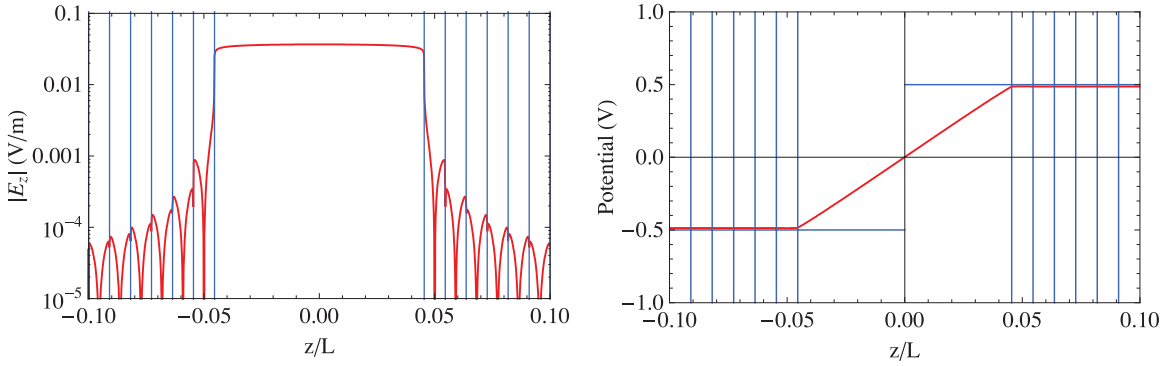

Fig. 2.2.11 Field E_z and integrated potential over the source region of the dipole when the ratio of source segment length to adjacent segment lengths Δ_s/Δ is 10.0 in NEC–4.

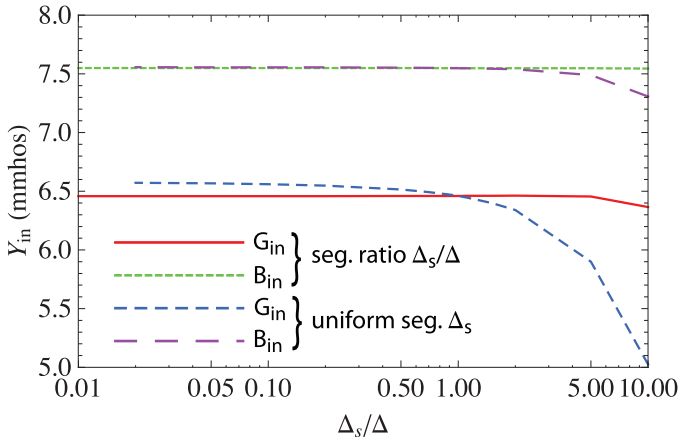

Fig. 2.2.12 Input admittance of a 0.475λ dipole with radius $10^{-6}\lambda$ computed with NEC–5 with the source segment length Δ_s and other segment lengths Δ, and also with uniform segment length Δ_s.

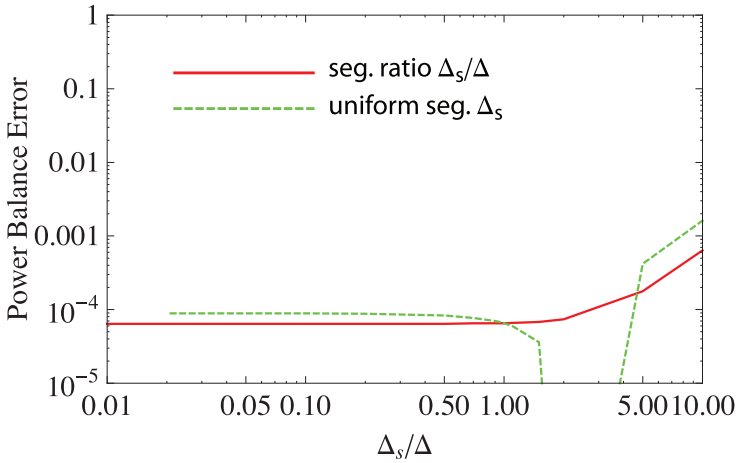

Fig. 2.2.13 Error in power balance $P_{\text{rad}}/P_{\text{in}}$ for a 0.475λ dipole with radius $10^{-6}\lambda$ computed with NEC–5 with the source segment length Δ_s and other segment lengths Δ, and also with uniform segment length Δ_s.

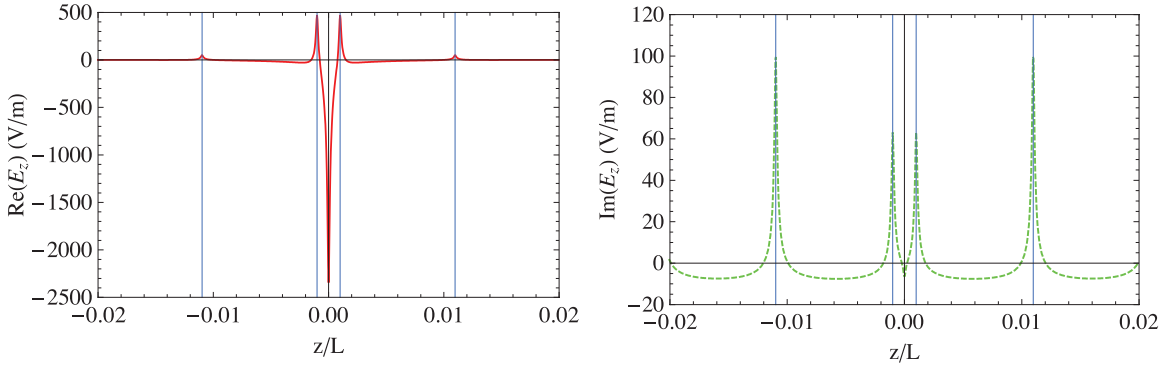

Fig. 2.2.14 Field E_z over the source region of a 0.5λ dipole with radius $10^{-4}\lambda$ from the NEC–5 solution with $\Delta_s/\Delta = 0.1$.

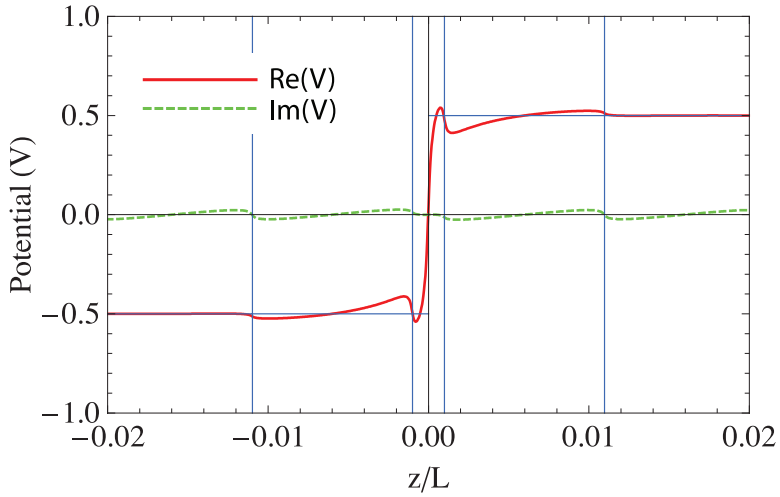

Fig. 2.2.15 Potential from integrating $-E_z$ in Fig. 14 for $\Delta_s/\Delta = 0.1$.

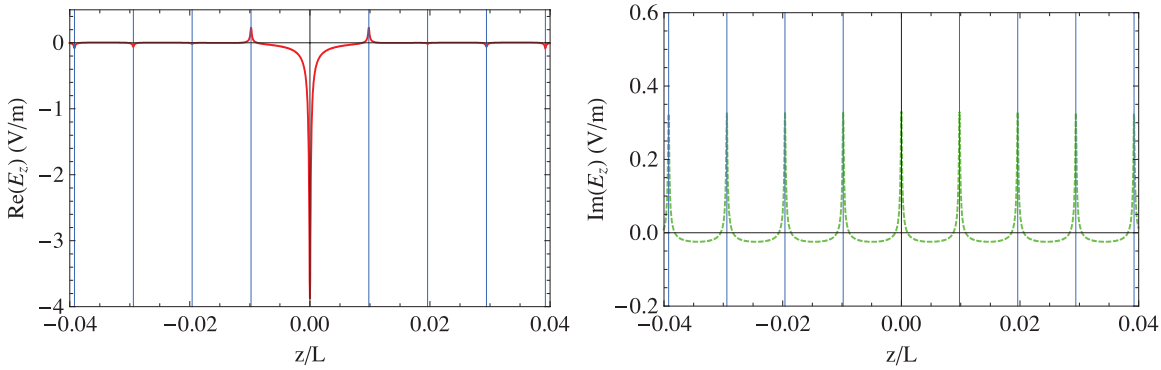

Fig. 2.2.16 Field E_z over the source region of a 0.5λ dipole with radius $10^{-4}\lambda$ from the NEC–5 solution with $\Delta_s/\Delta = 1$.

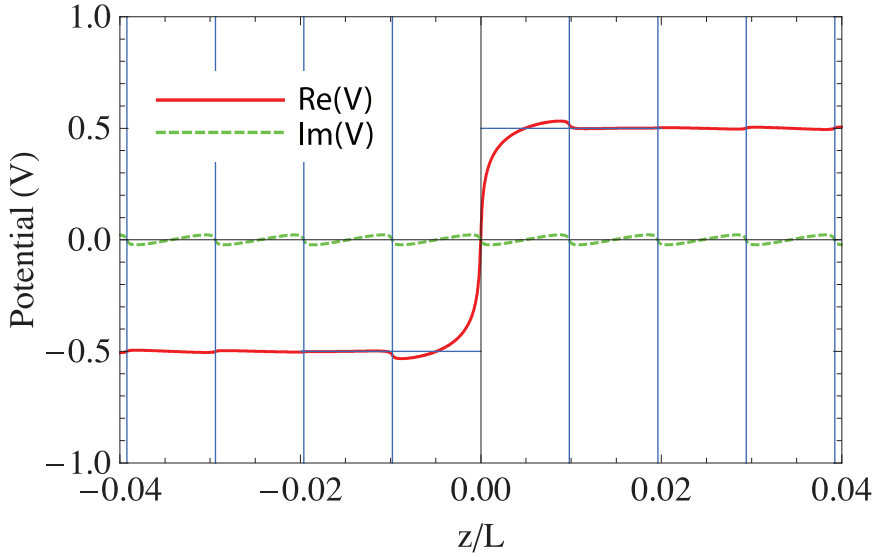

Fig. 2.2.17 Potential from integrating $-E_z$ in Fig. 16 for $\Delta_s/\Delta = 1$.

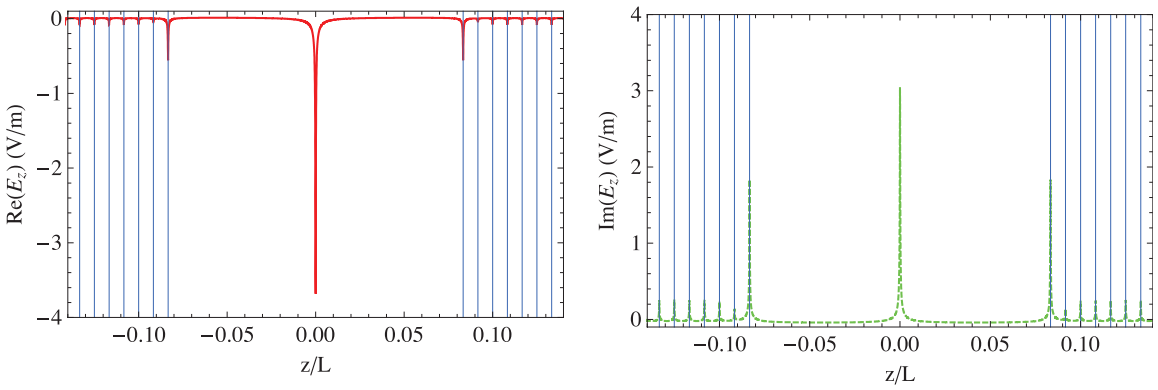

Fig. 2.2.18 Field E_z over the source region of a 0.5λ dipole with radius $10^{-4}\lambda$ from the NEC–5 solution with $\Delta_s/\Delta = 10$.

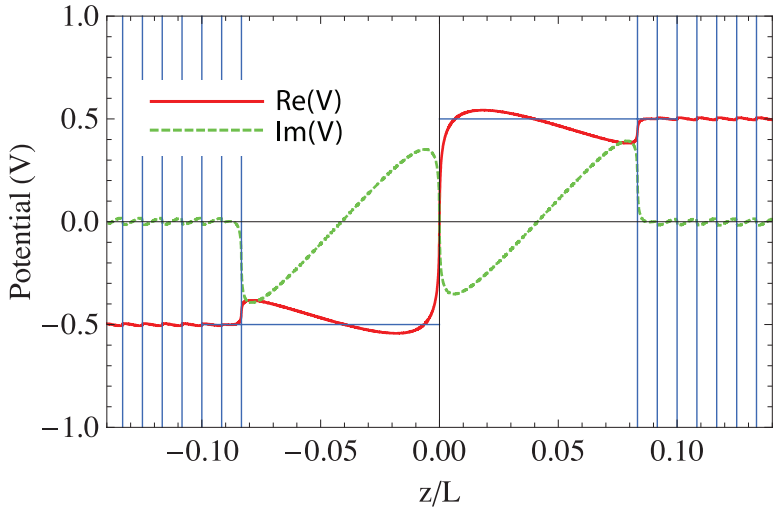

Fig. 2.2.19 Potential from integrating $-E_z$ in Fig. 18 for $\Delta_s/\Delta = 10$.

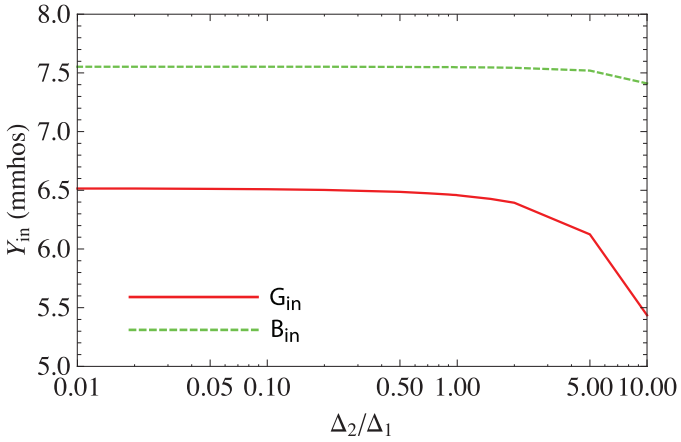

Fig. 2.2.20 Input admittance of a 0.475λ dipole with $(10^{-6})\lambda$ radius. Half of the dipole is modeled with 50 segments of length $\Delta_1 = 0.00475\lambda$ and the other half has segments of length Δ_2, with the change taking place across the voltage source..

2.3 Convergence for a Dipole Antenna

Results demonstrating the convergence of the solution for dipole antennas of varying thickness modeled with varying numbers of segments are shown in this section. Results from the King-Middleton second-order solution from [20] are included for reference.

Fig. 1 through 5 are the input admittance obtained with NEC–5. The admittance is seen to converge rapidly at the first resonance and more slowly at the second resonance. For thicker wires the susceptance becomes more capacitive with increasing number of segments N due to the increased effective shunt capacitance of the source gap. The input impedance, plotted in Fig. 6 through 10, shows slower convergence at the peaks since the change in susceptance due to gap width affects both real and imaginary parts of impedance. These anti-resonant points typically show slow convergence in method of moments solutions.

The same sequence of plots is repeated in Fig. 11 through 20 for NEC–4 results. The admittance peaks are seen to converge very rapidly in NEC–4, probably due to the sinusoidal current expansion. For higher numbers of segments on thick wires the NEC–4 solution starts to fail due to use of the reduced kernel.

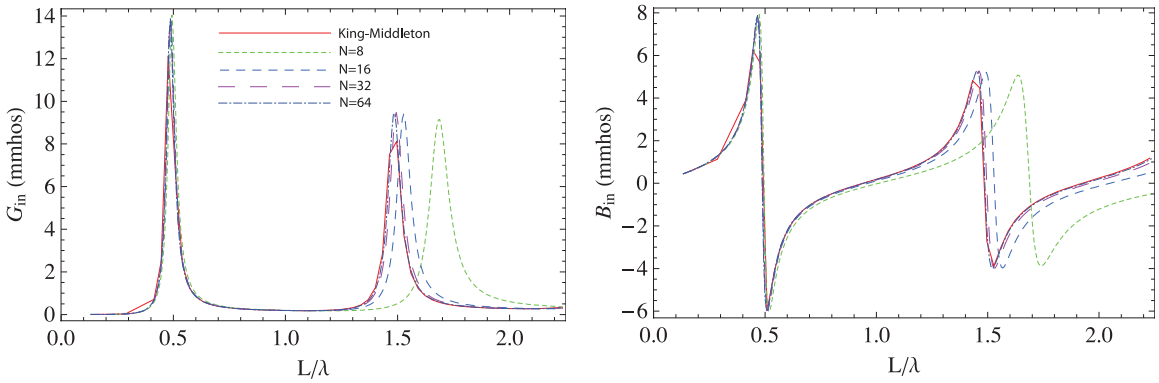

Fig. 2.3.1 Input admittance of a dipole with thickness factor $\Omega = 2\ln L/a = 20$ ($L/a = 22026$) modeled with NEC–5 with N segments.

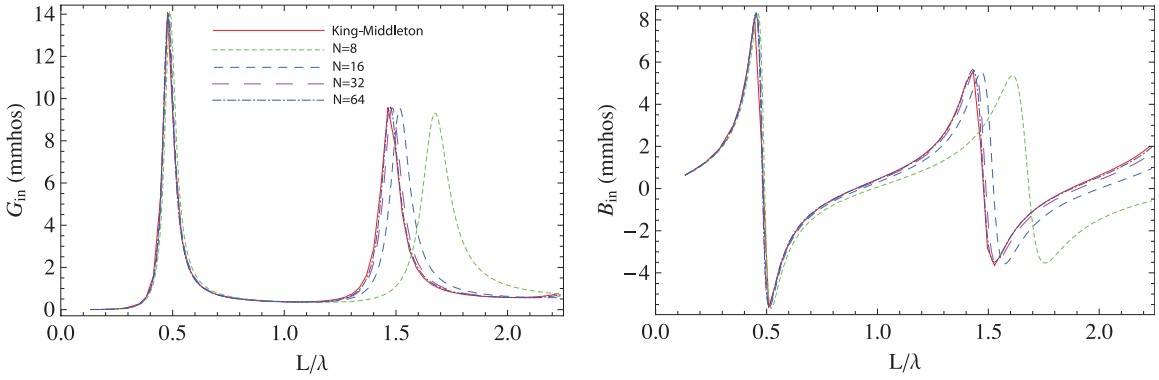

Fig. 2.3.2 Input admittance of a dipole with thickness factor $\Omega = 2\ln L/a = 15$ ($L/a = 1808$) modeled with NEC–5 with N segments.

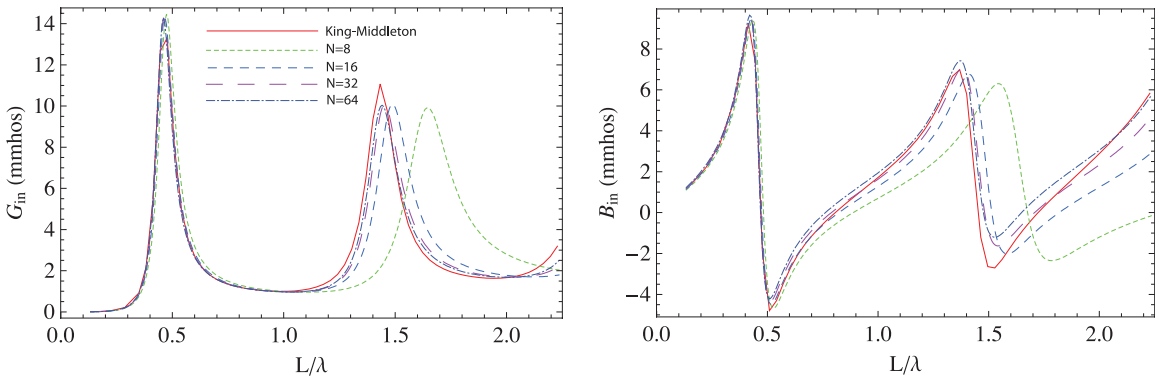

Fig. 2.3.3 Input admittance of a dipole with thickness factor $\Omega = 2\ln L/a = 10$ ($L/a = 148.41$) modeled with NEC–5 with N segments.

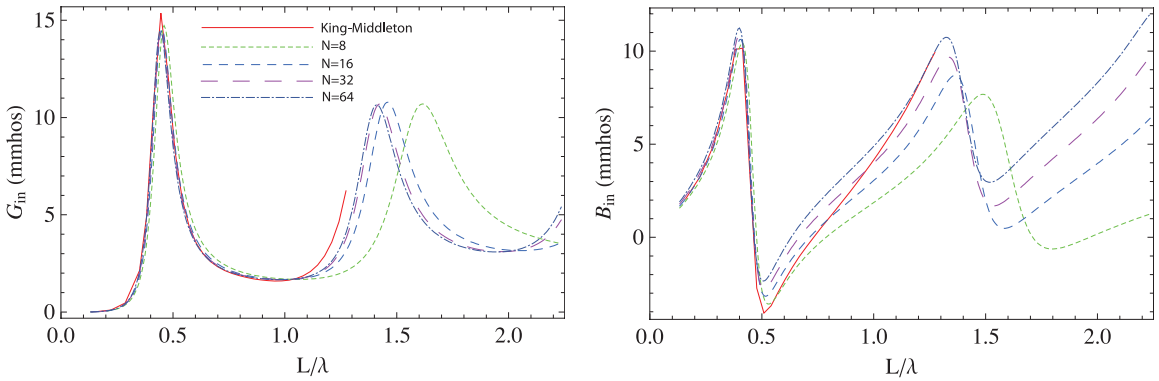

Fig. 2.3.4 Input admittance of a dipole with thickness factor $\Omega = 2\ln L/a = 8$ ($L/a = 54.60$) modeled with NEC–5 with N segments.

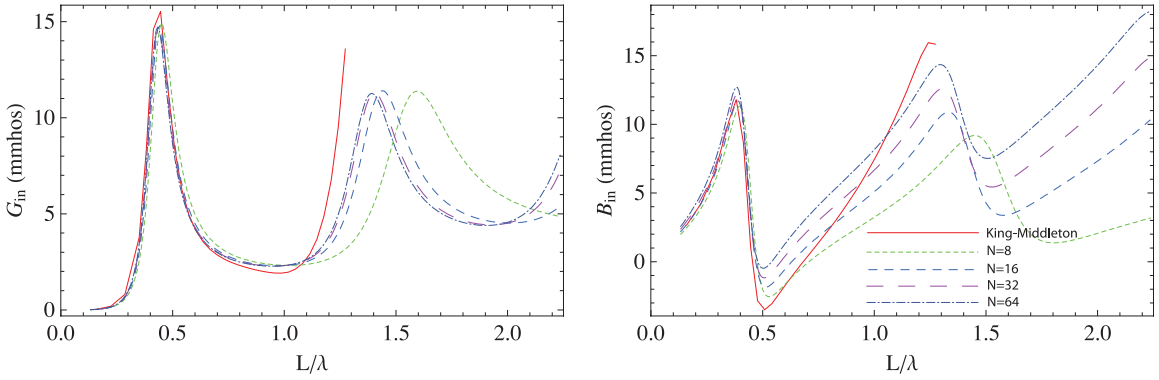

Fig. 2.3.5 Input admittance of a dipole with thickness factor $\Omega = 2\ln L/a = 7$ ($L/a = 33.12$) modeled with NEC–5 with N segments.

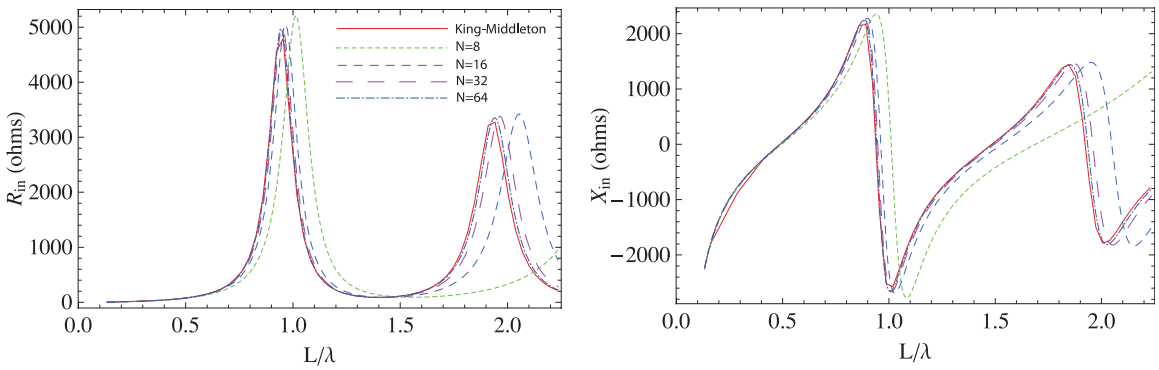

Fig. 2.3.6 Input impedance of a dipole with thickness factor $\Omega = 2\ln L/a = 20$ ($L/a = 22026$) modeled with NEC–5 with N segments.

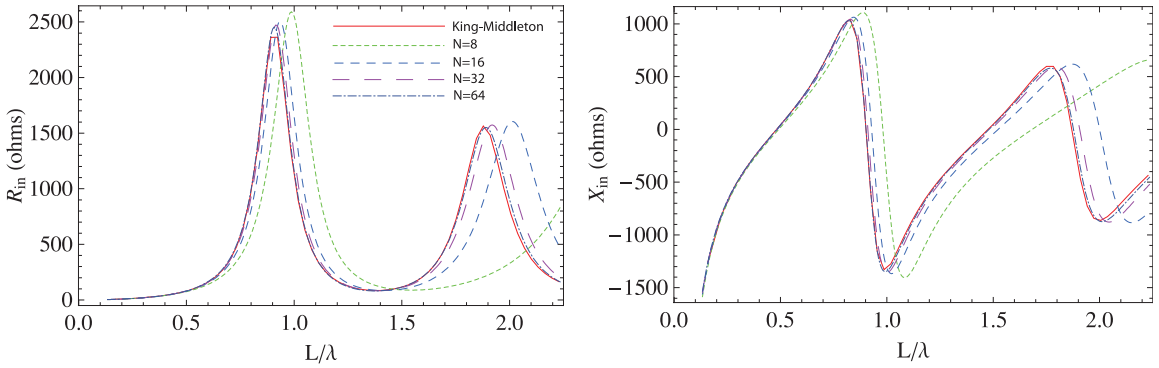

Fig. 2.3.7 Input impedance of a dipole with thickness factor $\Omega = 2\ln L/a = 15$ ($L/a = 1808$) modeled with NEC–5 with N segments.

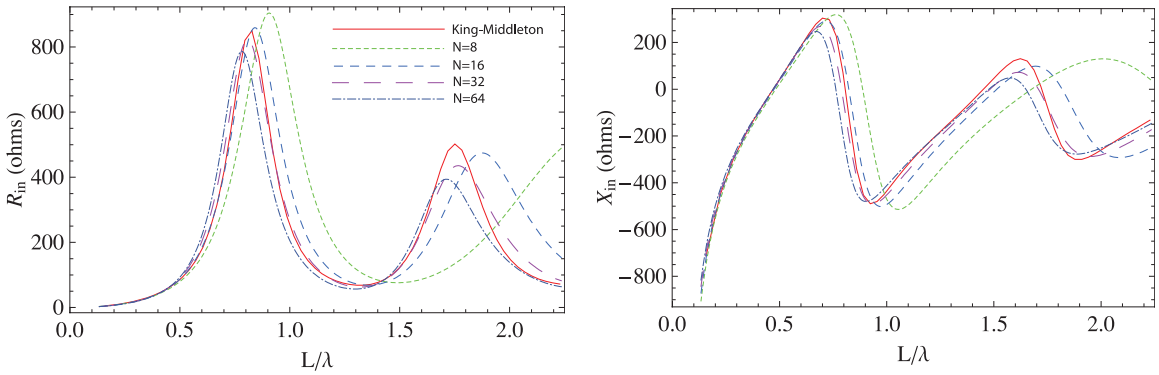

Fig. 2.3.8 Input impedance of a dipole with thickness factor $\Omega = 2\ln L/a = 10$ ($L/a = 148.41$) modeled with NEC–5 with N segments.

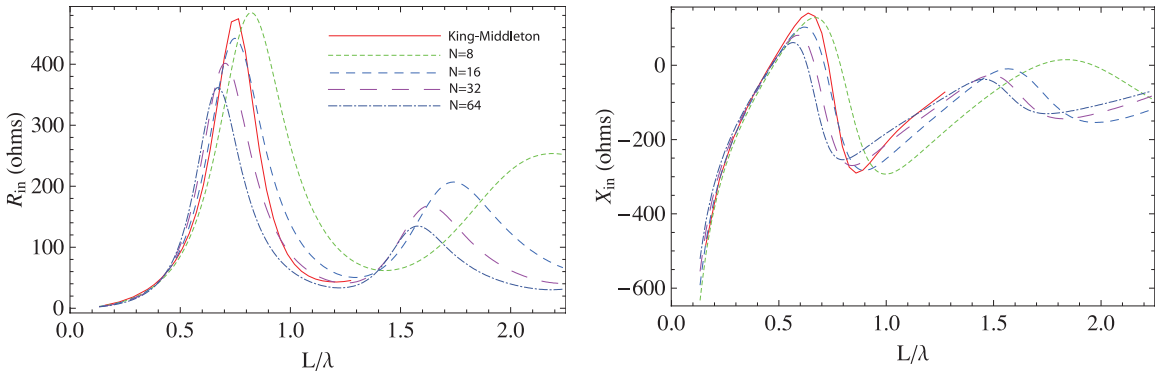

Fig. 2.3.9 Input impedance of a dipole with thickness factor $\Omega = 2\ln L/a = 8$ ($L/a = 54.60$) modeled with NEC–5 with N segments.

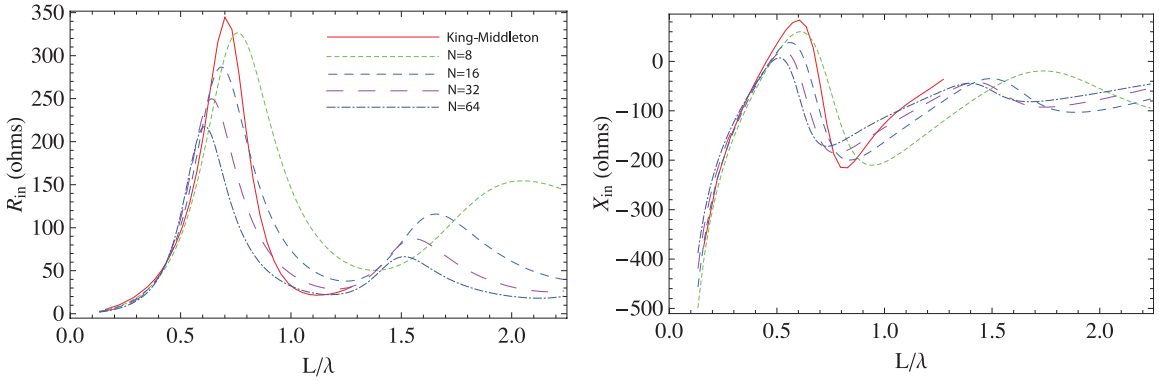

Fig. 2.3.10 Input impedance of a dipole with thickness factor $\Omega = 2\ln L/a = 7$ ($L/a = 33.12$) modeled with NEC–5 with N segments.

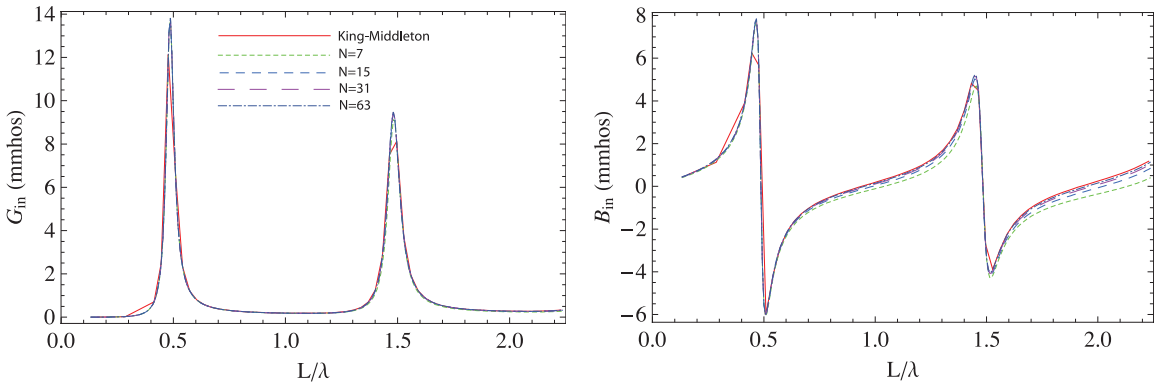

Fig. 2.3.11 Input admittance of a dipole with thickness factor $\Omega = 2\ln L/a = 20$ ($L/a = 22026$) modeled with NEC–4 with N segments.

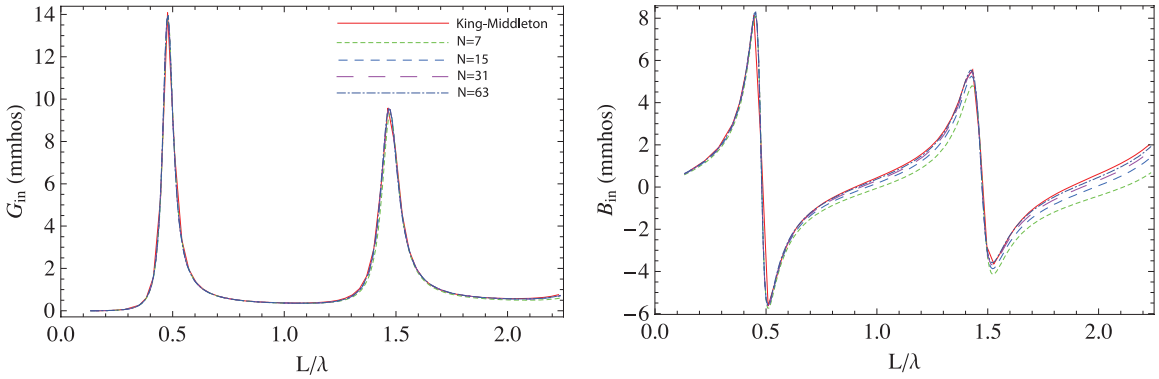

Fig. 2.3.12 Input admittance of a dipole with thickness factor $\Omega = 2\ln L/a = 15$ ($L/a = 1808$) modeled with NEC–4 with N segments.

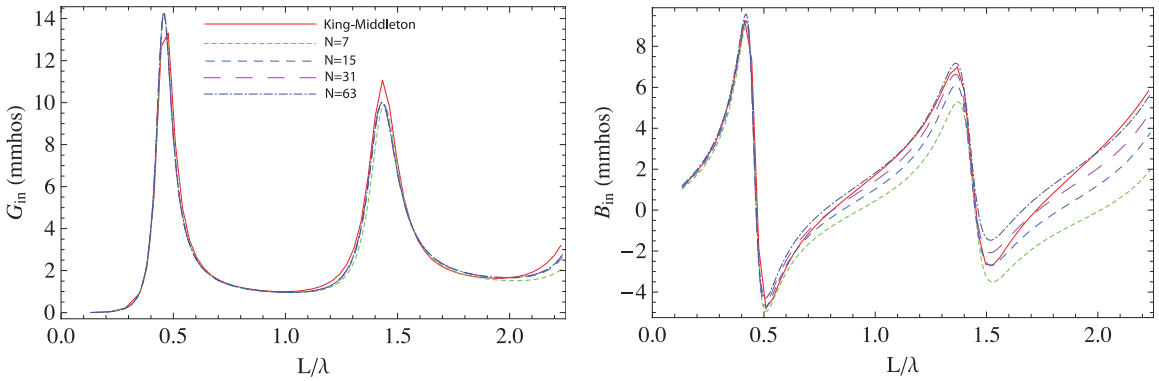

Fig. 2.3.13 Input admittance of a dipole with thickness factor $\Omega = 2\ln L/a = 10$ ($L/a = 148.41$) modeled with NEC–4 with N segments.

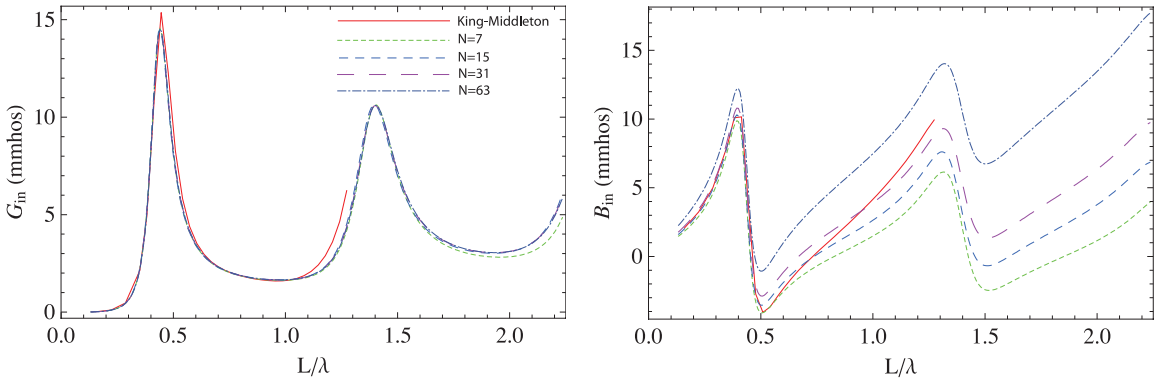

Fig. 2.3.14 Input admittance of a dipole with thickness factor $\Omega = 2\ln L/a = 8$ ($L/a = 54.60$) modeled with NEC–4 with N segments.

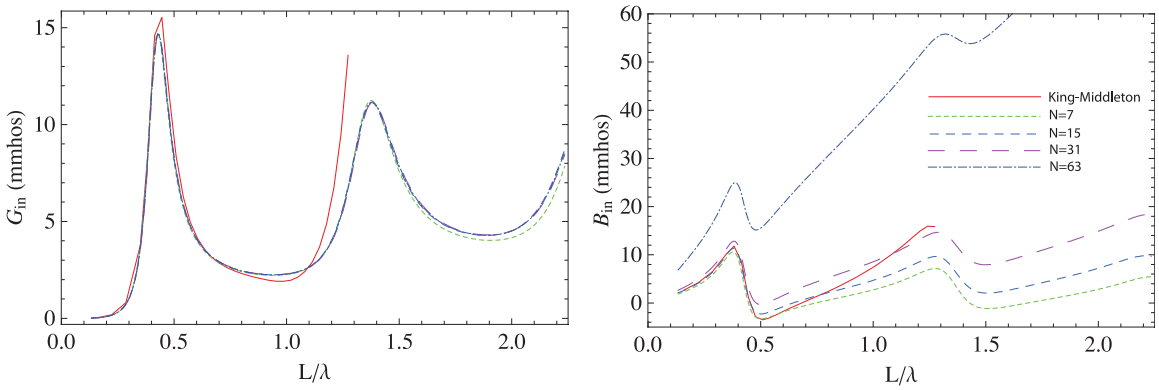

Fig. 2.3.15 Input admittance of a dipole with thickness factor $\Omega = 2\ln L/a = 7$ ($L/a = 33.12$) modeled with NEC–4 with N segments.

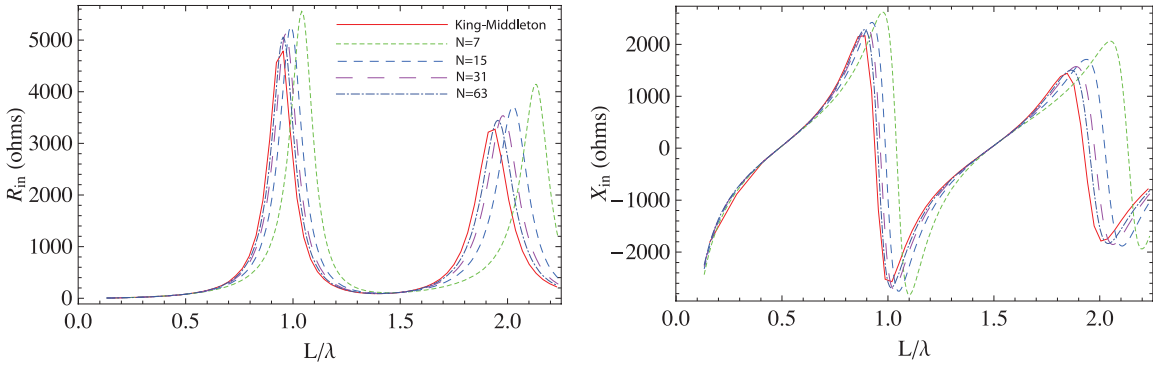

Fig. 2.3.16 Input impedance of a dipole with thickness factor $\Omega = 2\ln L/a = 20$ ($L/a = 22026$) modeled with NEC–4 with N segments.

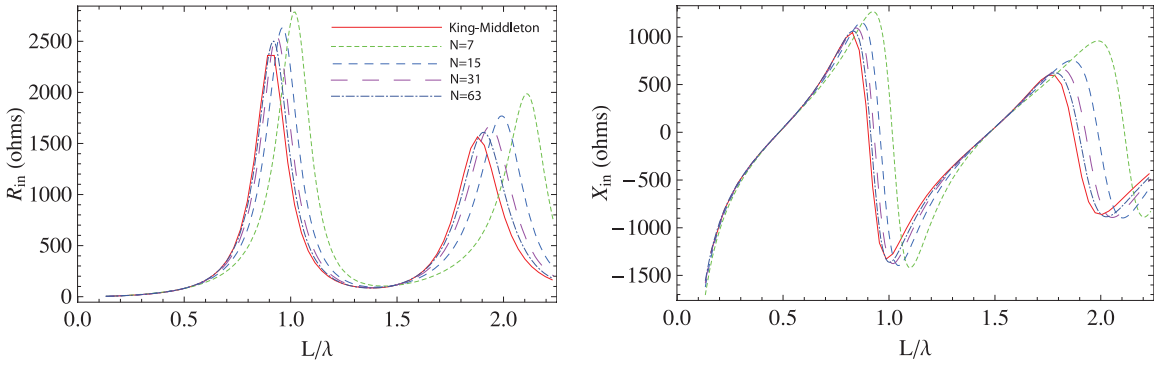

Fig. 2.3.17 Input impedance of a dipole with thickness factor $\Omega = 2\ln L/a = 15$ ($L/a = 1808$) modeled with NEC–4 with N segments.

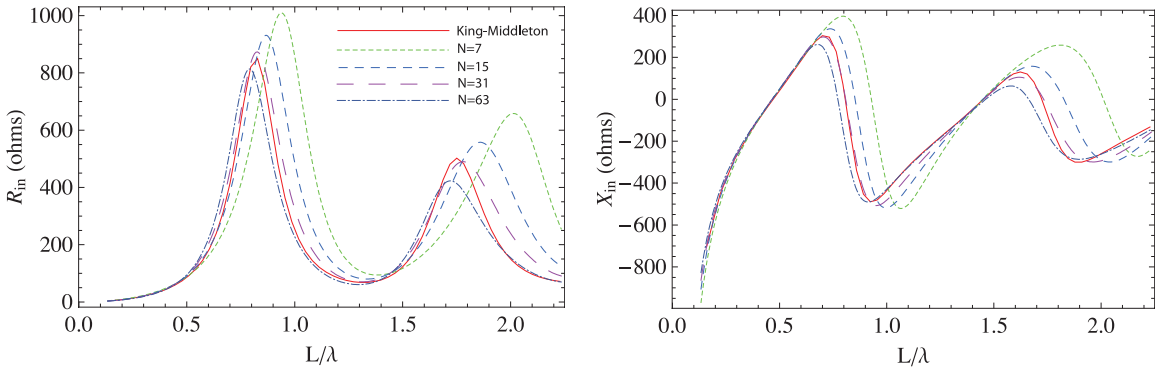

Fig. 2.3.18 Input impedance of a dipole with thickness factor $\Omega = 2\ln L/a = 10$ ($L/a = 148.41$) modeled with NEC–4 with N segments.

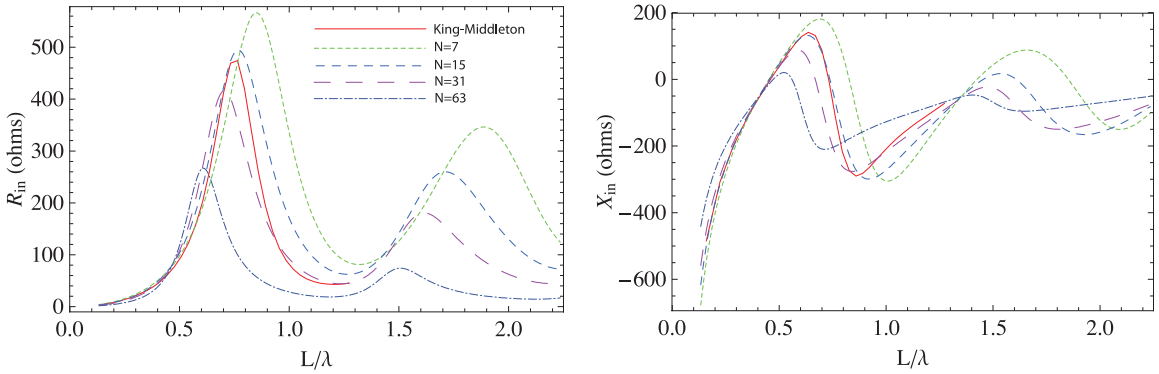

Fig. 2.3.19 Input impedance of a dipole with thickness factor $\Omega = 2\ln L/a = 8$ ($L/a = 54.60$) modeled with NEC–4 with N segments.

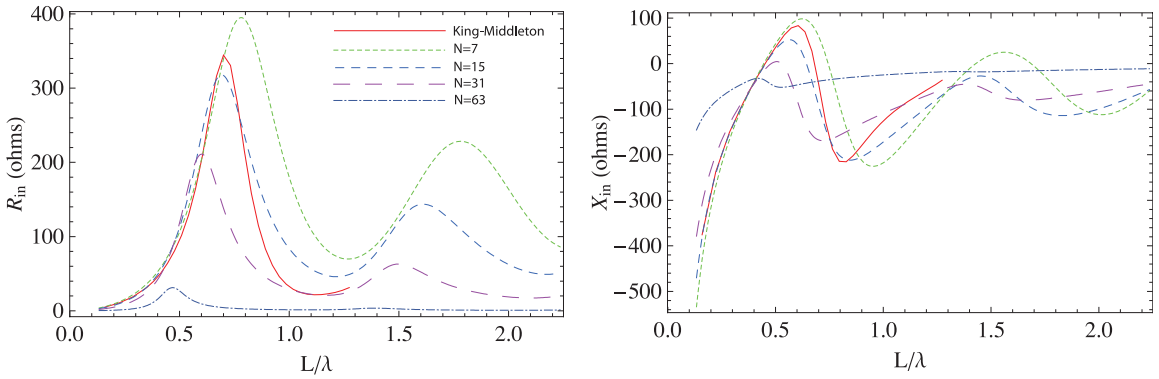

Fig. 2.3.20 Input impedance of a dipole with thickness factor $\Omega = 2\ln L/a = 7$ ($L/a = 33.12$) modeled with NEC–4 with N segments.

2.4 Wire Loops

Electrically small loops are a problem with both NEC–4 and 5 and any code that uses localized basis and weighting functions, since the matrix becomes ill-conditioned at low frequencies as the current becomes uniform around the loop. The input admittances of a loop modeled in NEC–4 and 5 down to $C/\lambda = 10^{-8}$ are shown in Fig. 1. The input susceptance $B_{\rm in}$ should increase as the inverse of C/λ at low frequencies. $B_{\rm in}$ fails in NEC–4 at around $C/\lambda = 10^{-6}$. NEC–5 goes a little further with susceptance, but fails also. The $G_{\rm in}$ result fails in NEC–5 above $C/\lambda = 10^{-4}$ when it is about 10^{-12} below $B_{\rm in}$, while NEC–4 goes to almost $C/\lambda = 10^{-6}$. A considerable effort was put into NEC–4 to preserve the real part when it gets small relative to the imaginary part. A similar effort might extend the NEC–5 solution.

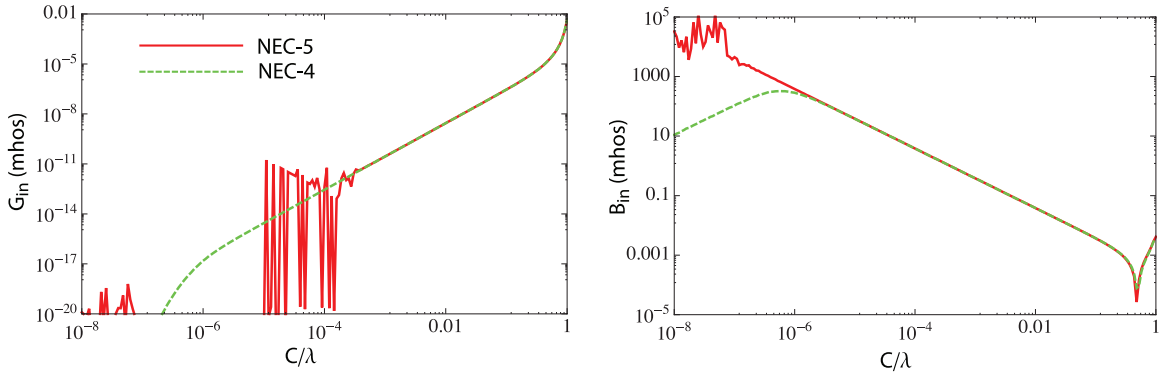

Fig. 2.4.1 Input admittance of a loop antenna with circumference C and wire radius $1.59(10^{-4})C$ modeled with 22 segments in NEC–4 and 5.

A weakness of NEC–4 is the instability of currents in small loops that are coupled to driven structures. A typical problem is illustrated in Fig. 2, where a driven dipole is near a loop that does not contain a source. At low frequencies the electric field of the dipole is dominated by the gradient of scalar potential ($\nabla\phi$) from the charge at its ends. Since $\nabla\phi$ has zero curl, the integral of this term around the loop must be zero. NEC–4 evaluates the electric field accurately at the match points on the segments, but does not take into account the variation between match points. The resulting error in sampling $\nabla\phi$ appears as a voltage in the loop and can drive a current proportional to one over frequency, while the loop current should go to zero with frequency.

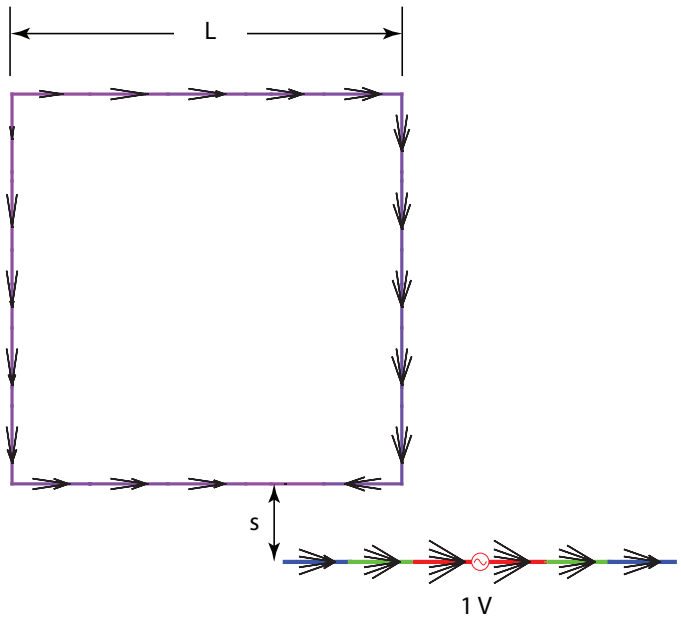

Fig. 2.4.2 NEC–5 result for the imaginary part of current on a square loop coupled to a dipole antenna with $s/L = 0.2$ and $C = 4L = 4(10^{-5})\lambda$.

In the mixed-potential solution in NEC–5 the potentials are also evaluated only at the segment centers. However, the $\nabla\phi$ term is approximated as differences between ϕ at successive center points, so the sum of the $\nabla\phi$ approximations around a closed loop is zero to machine accuracy. The mixed-potential solution will also fail at a low enough frequency as the matrix becomes ill-conditioned. But the mixed-potential method can go orders of magnitude lower in frequency than NEC–4 in this type of problem.

The accuracy of the NEC–4 solution can be improved by evaluating the field at more than one point on each segment and approximating the integral of **E** over the segments. A version of NEC–4 was set up to evaluate the field at a variable number of points on each segment and apply a Gauss-Legendre rule for the integral.

Results for the current on the loop in Fig. 2 are plotted in Fig. 3 as frequency is decreased until the circumference C of the loop is about $4(10^{-5})\lambda$. The NEC–4 solution is seen to blow up for C/λ just less than 1. Integrating with up to 9 points per segment in the modified NEC–4 reduces the frequency where it fails by about an order of magnitude, but at the expense of increased time to fill the matrix. The NEC–5 solution shows the correct decrease of loop current with frequency through the range of the plot.

NEC-SL [21] is a version of NEC–4 that was modified to find loops and replace one basis function in each loop with a constant current around the loop and replace one match point with a loop weighting function. The NEC-SL result also remains stable through the range of the plot. However, it is difficult to implement this solution for complex structures, since all loops must be found and care is needed in handling loop that share common sides. The NEC–SL code was never developed to the point that it could be released.

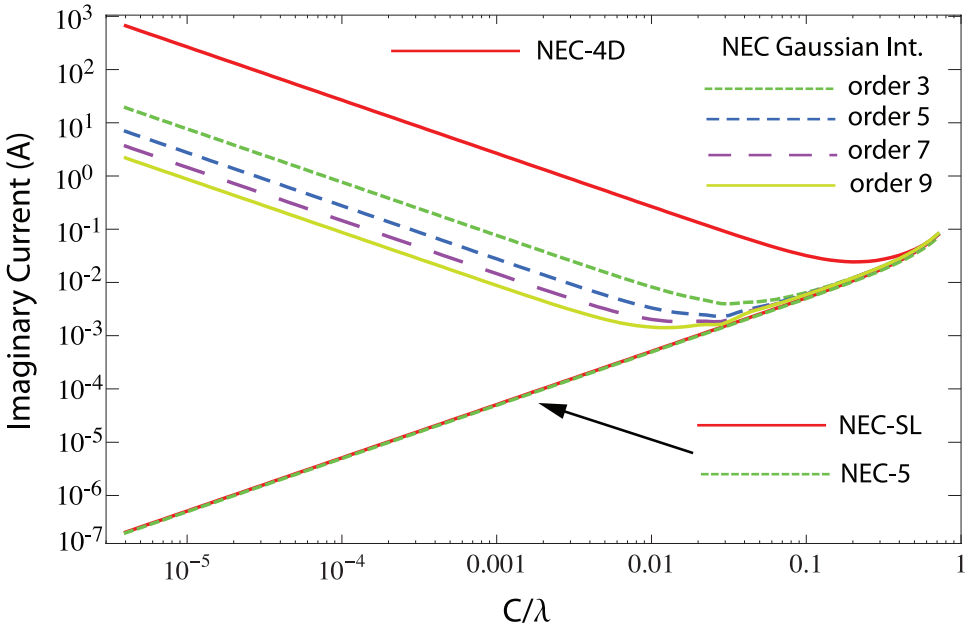

Fig. 2.4.3 Current at the center of the near side of the loop in Fig. 2 versus frequency, showing the low frequency blow up of current with NEC–4 and the stable solution with NEC–5.

3. Wire-Surface Junctions

Modeling surfaces and wire-surface junctions has been a major weakness of NEC–4 where surface models use the MFIE which is limited to closed, perfectly conducting surfaces. The MFIE model as implemented in NEC–4 works well for scattering by a sphere and reasonably well for a box, but attempts to model even a moderately thin plate as a box with one thin dimension may not be handled accurately. NEC–4 is fast in filling the MFIE matrix due to the use of point matching and single-point integration. In modeling ship hulls it was found to give reasonable accuracy in radiation patterns, but is not accurate for impedances of connected wire antennas.

Connection of a wire modeled with the EFIE in NEC–4 to a MFIE surface is particularly problematic. A wire is connected at the center of a patch which is split into four sub-patches and a singular basis function is used to join the surface current to the wire current using the method in [22]. As seen in the results that follow, the impedance at a wire-surface junction may have reasonable accuracy if the wire segment length is in the right range relative to the patch size, but the solution is not reliable. As a result, wire-surface junctions are often modeled using a wire grid surface in NEC–4. This approach has its own problems with small loops and other issues.

NEC–5 uses the mixed potential formulation for both wires and surfaces with triangular or roof-top basis functions as developed by Rao,Wilton and Glisson [4] and a singularl basis function at a wire-surface junction as developed by Rao [8] and Costa and Harrington [9, 10]. This treatment appears to be stable and accurate. NEC–5 results are compared here with measurements by Bhattacharya, Long and Wilton [23]. Subsequent plots compare NEC–4 results for varying segmentation using NEC-5 as a standard.

3.1 The Monopole on a Box

An extensive set of measurements has been reported in [23, 24] for impedance and radiation patterns of monopoles on a 10 cm box. These results have often been used in the past in validating wire-surface junction models. The basic model, shown in Fig. 1, is a cube 10 cm on a side with monopoles of various lengths and radius 0.8 mm located at positions on the top. NEC–5 has been tested for a 6 cm monopole at the center and near one corner. In the measurements the box was on a 78×78 cm ground plane, while the model used an infinite ground plane.

Fig. 1 shows the currents computed with NEC–5 for the 6 cm monopole at the center of the top at 1.15 GHz. The arrows show the real part of current over three orders of magnitude range, and the color represents the magnitude of current at the center of each element on a log scale covering two orders of magnitude from red to violet. Current is shown on wires and surface current density on patches, so they are not directly comparable. The currents at 1.15 GHz with the 6 cm monopole near a corner, displaced 5.15 cm from the center, are shown in Fig. 2.

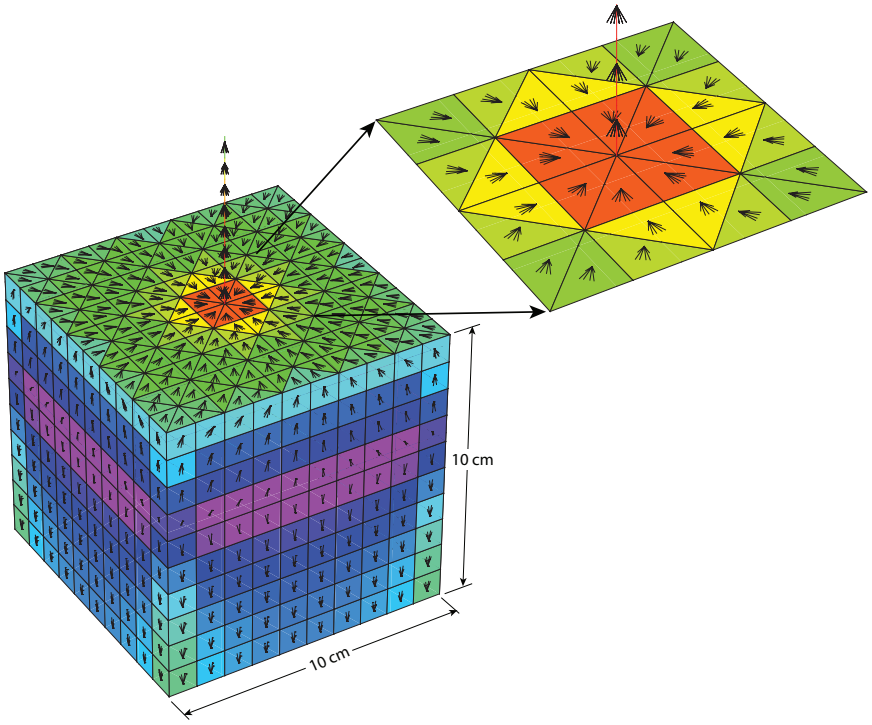

Fig. 3.1.1 Current on a 10 cm box with a 6 cm monopole at the center of the top at 1.15 GHz. Arrows show the real part of wire current or surface current density and color represents the magnitude.

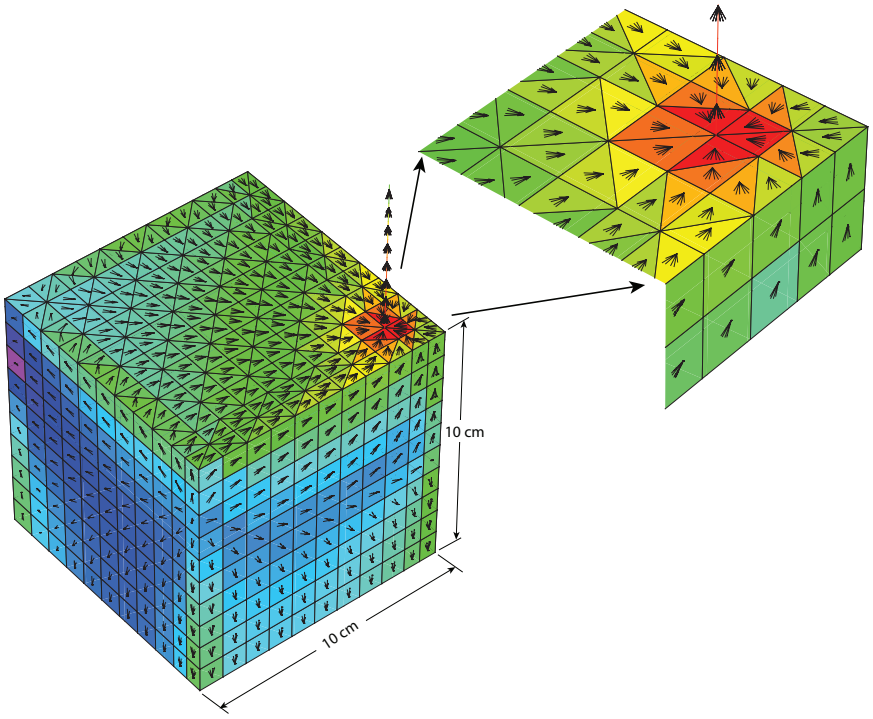

Fig. 3.1.2 Current on a 10 cm box with a 6 cm monopole near the corner, displaced 5.15 cm from the center, at 1.15 GHz.

The input admittances from NEC–5 for the 6 cm monopole at the center position are plotted in Fig. 3. The measured results were read as accurately as possible from [23]. The NEC–5 model 1 had 10 by 10 divisions of triangular patches on the top and 10 by 10 rectangular patches on the sides, with 8 segments on the monopole, as shown in Fig. 1. Model 2 had 20 by 20 divisions on top and sides and 16 segments on the monopole. The convergence is seen to be good in the NEC–5 results, with a slight frequency shift from measurements. The admittance with the monopole at the corner position, 5.15 cm from the center, is plotted in Fig. 4. Model 1 was as shown in Fig. 2, and model 2 had 20 by 20 divisions on continuous sides with 18 between the wire and the far sides and 3 between the wire and the near sides with 16 segments on the wire. Again, there is a slight frequency shift from measured results but good convergence.

The monopole at the center of the box was also modeled with the NEC–4 patch model. The first model had 11 by 11 patches on each side and the top, and the monopole was modeled with N_m segments. The results in Fig. 5 show a strong dependence on the wire segment length. The best agreement is obtained with segments about equal in length to the patch widths, although the agreement is not great. A different view of the result is seen in the impedance plots in Fig. 6. At low frequencies the agreement in resistance is not bad, but a large capacitive reactance error is added as the wire segments are made shorter. Another NEC–4 model was run with 11 by 11 patches on the four sides and 21 by 21 on the top. This can be done in NEC–4, since the patches do not have to have matching edges as in the NEC–5 mixed-potential solution. The admittance and impedance results for this higher resolution model are shown in Fig. 7 and 8. The best agreement is now obtained with 10 segments on the monopole. It may be best in NEC–4 models to make the wire segments as long as possible at the connection point. These results are consistent with previous observations that the NEC–4 patch model may give useable accuracy for some purposes with the advantage of a fast matrix fill for the MFIE matrix elements.

The radiation patterns from NEC–5 for the 6 cm monopole at the center of the box at 1.138 GHz are shown in Fig. 9. The horizontal radiation (E_ϕ) would be zero for the monopole on an infinite ground plane, but a small horizontal component is introduced by the box. Since it is down by 42.7 dB from the vertical gain, the horizontal pattern is sensitive to asymmetries in the mesh. Fig. 10 shows the mesh patterns and resulting current magnitudes for values of the IALT parameter on the QP command from 0 through 3. The azimuthal radiation patterns resulting from these meshes are shown in Fig. 11. In this case the symmetric mesh patterns with IALT of 2 or 3 are the better choice. The power balance from integrating the radiated power was $P_{\rm rad}/P_{\rm in} = 0.990$ for IALT of 0 or 1, 0.986 for IALT = 2 and 0.994 for IALT = 3. Elevation patterns of vertical and horizontal gain in the $\phi = 22.5^\circ$ plane are shown in Fig. 12. These patterns agree with the computed patterns reported by Chu et al. in Fig. 15 of [24] and agree as well as can be expected with the measured patterns in [24].

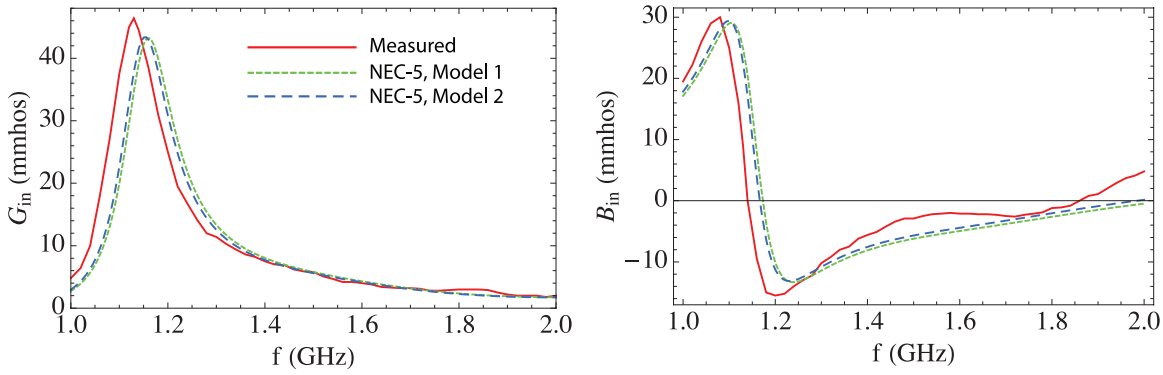

Fig. 3.1.3 Input admittance of the 6 cm monopole on the 10 cm box at the center position. Measured values were read from [23].

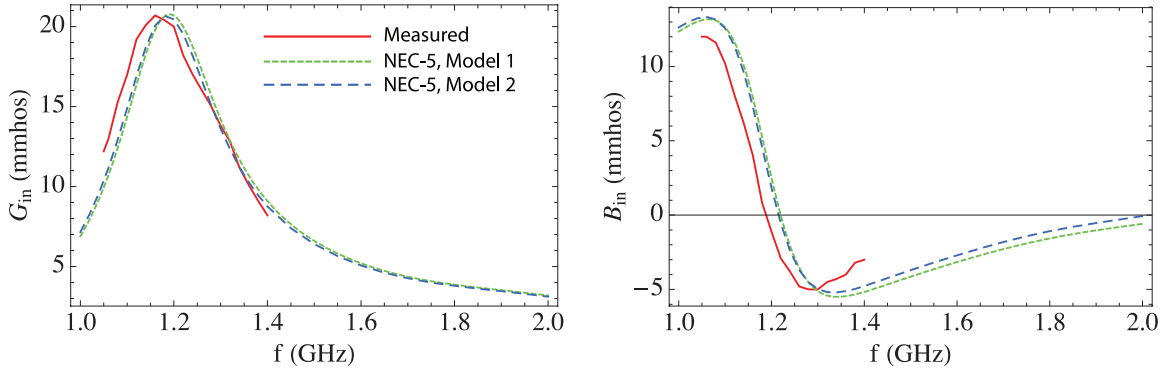

Fig. 3.1.4 Input admittance of the 6 cm monopole on the 10 cm box at the corner position, 5.15 cm from the center. Measured values were read from [23].

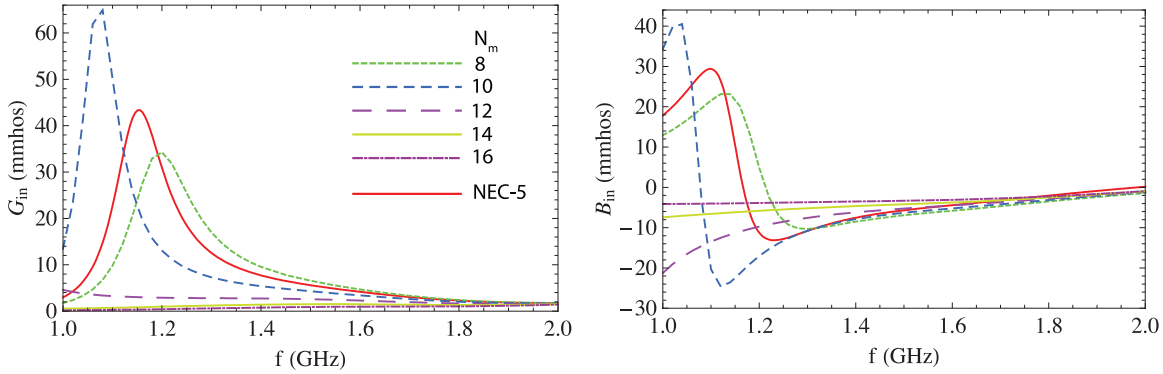

Fig. 3.1.5 Input admittance of the 6 cm monopole at the center position on the box from the NEC–4 patch model with N_m segments on the monopole and 11 by 11 patches on top and sides. The NEC–5 result from the model 2 mesh is included for comparison.

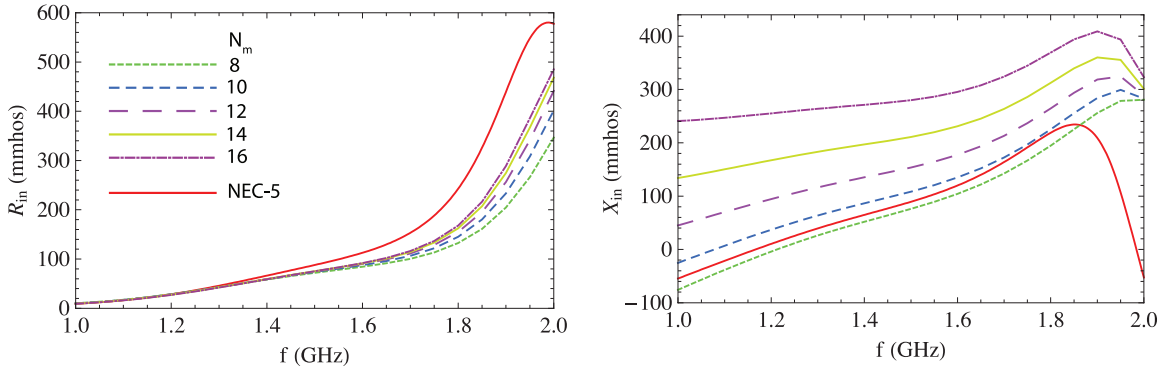

Fig. 3.1.6 Input impedance of the 6 cm monopole at the center position on the box from the NEC–4 patch model with N_m segments on the monopole and 11 by 11 patches on top and sides. The NEC–5 result from the model 2 mesh is included for comparison.

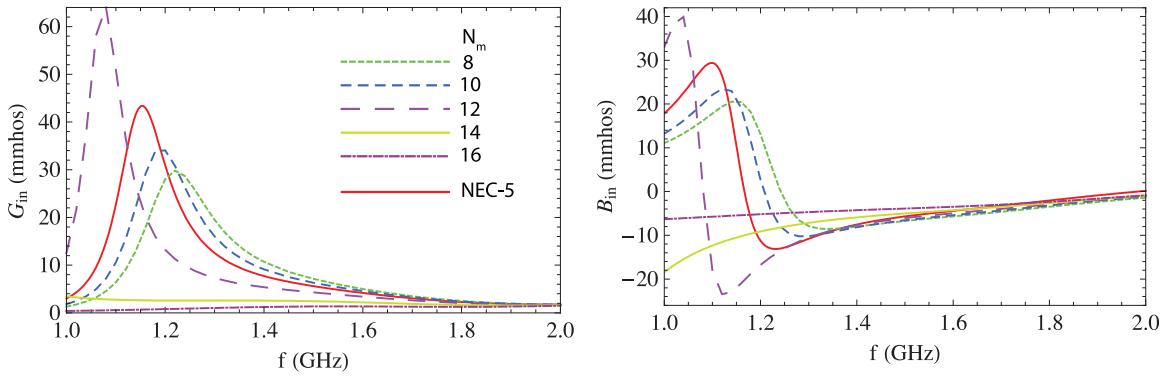

Fig. 3.1.7 Input admittance of the 6 cm monopole at the center position on the box from the NEC–4 patch model with N_m segments on the monopole, 21 by 21 patches on top and 11 by 11 on the sides. The NEC–5 result from the model 2 mesh is included for comparison.

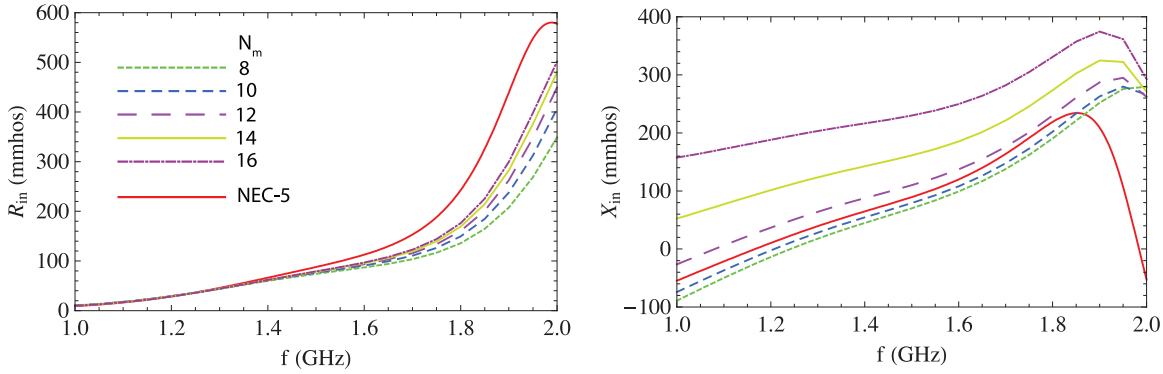

Fig. 3.1.8 Input impedance of the 6 cm monopole at the center position modeled with the NEC–4 patch model with N_m segments on the monopole, 21 by 21 patches on top and 11 by 11 on the sides. The NEC–5 result from the model 2 mesh is included for comparison.

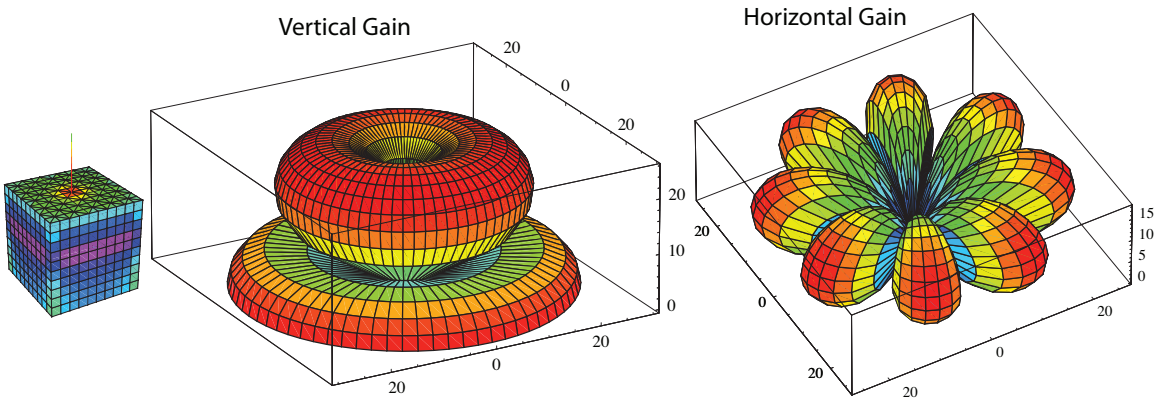

Fig. 3.1.9 Normalized gain patterns for the monopole at the center of the box at 1.138 GHz. The maximum directive gains are 5.85 dB for vertical polarization (E_θ) and -36.9 dB for horizontal polarization (E_ϕ).

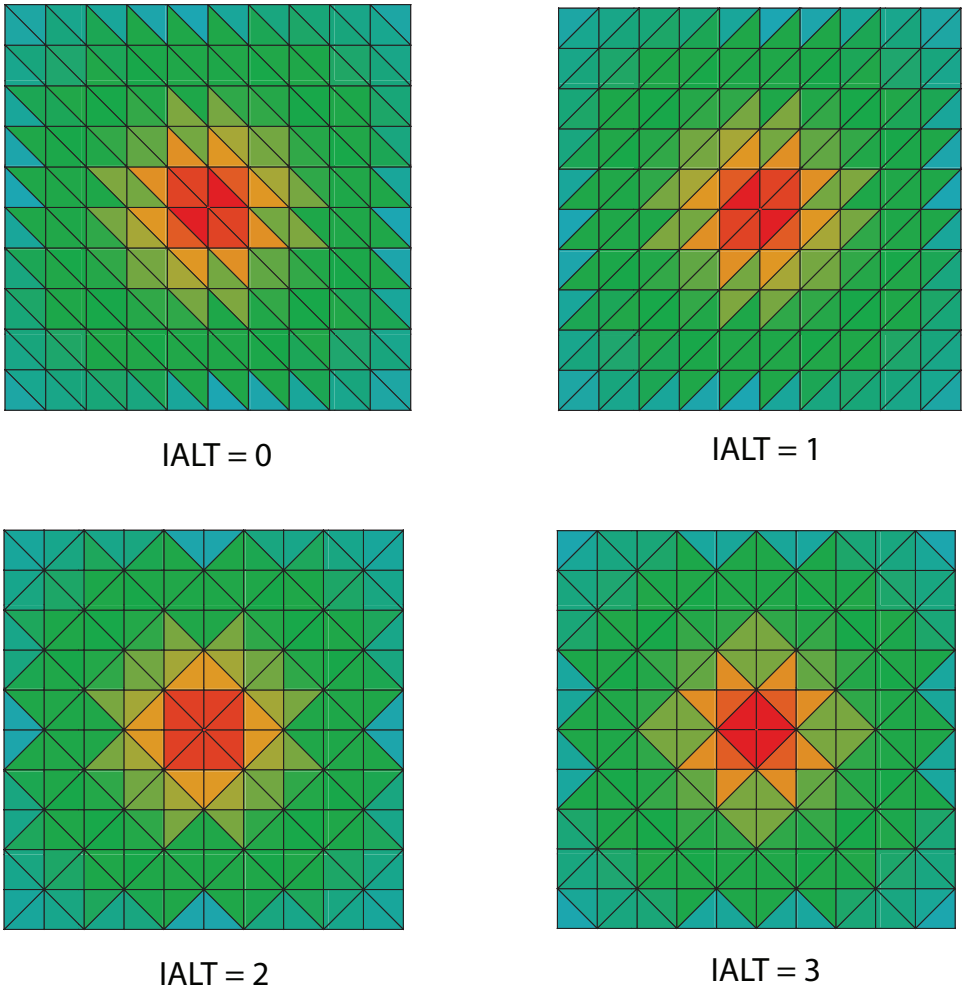

Fig. 3.1.10 Mesh patterns and current magnitudes obtained for the triangular patches on the top of the box with different values of IALT on the QP command.

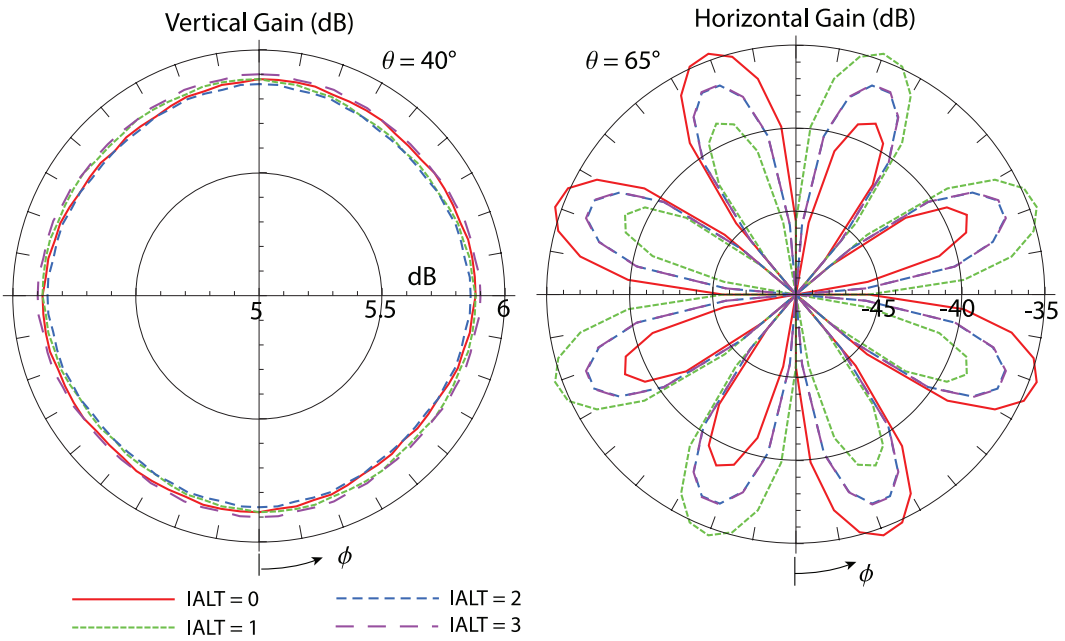

Fig. 3.1.11 Vertical and horizontal gain patterns in azimuth for the monopole at the center of the box at 1.15 GHz, showing the effect of the mesh patterns in Fig. 10.

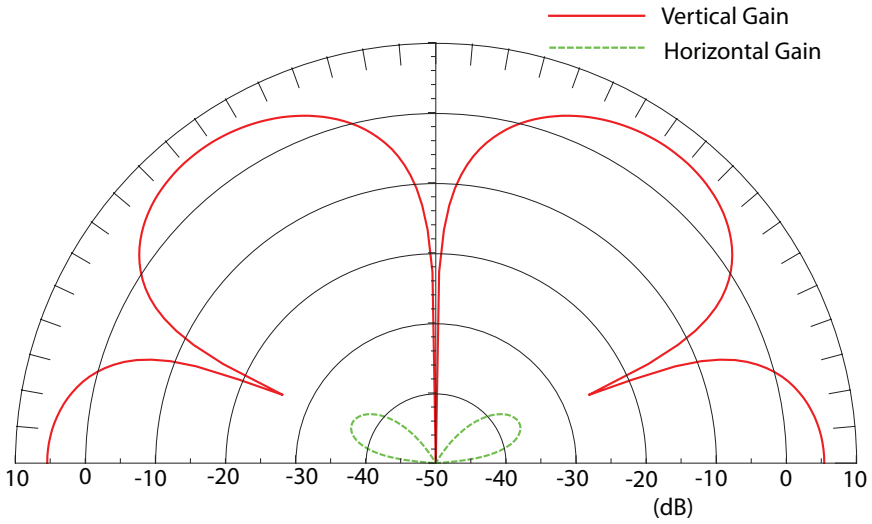

Fig. 3.1.12 Elevation patterns of vertical and horizontal gain in the $\phi = 22.5°$ plane for the monopole at the center of the box at 1.138 GHz.

The radiation patterns for the 6 cm monopole at the corner position on the box, 5.15 cm from the center, at 1.192 GHz are shown in Fig. 13. The power balance from integrating the radiated power was $P_{\text{rad}}/P_{\text{in}} = 0.987$. Elevation patterns of gain in the $\phi = 45°$ and $-45°$ planes are shown in Fig. 14. The pattern in the $\phi = -45°$ plane matches the computed pattern in Fig. 17 of [24] and is in reasonable agreement with the measured pattern in that paper.

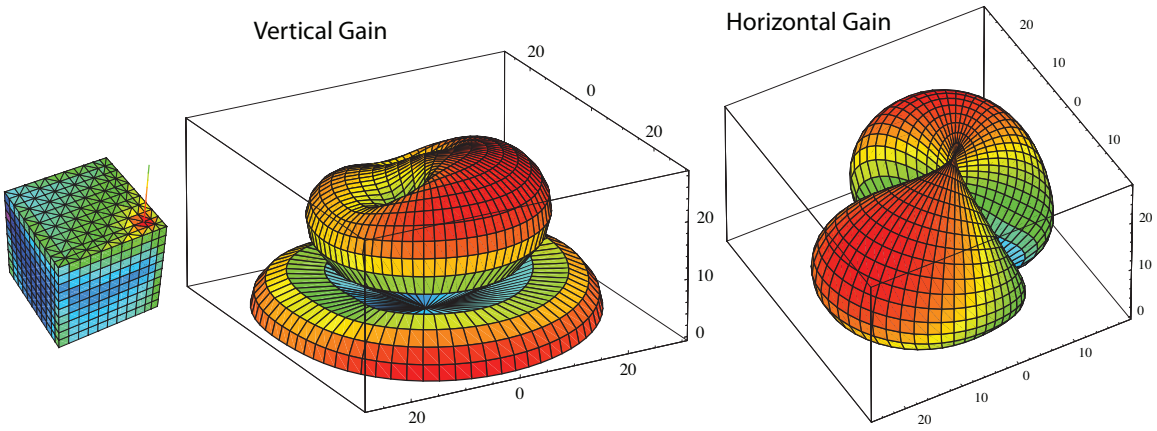

Fig. 3.1.13 Normalized gain patterns for the monopole at the corner position on the box at 1.192 GHz. The maximum directive gains are 5.14 dB for vertical polarization (E_θ) and 4.59 dB for horizontal polarization (E_ϕ).

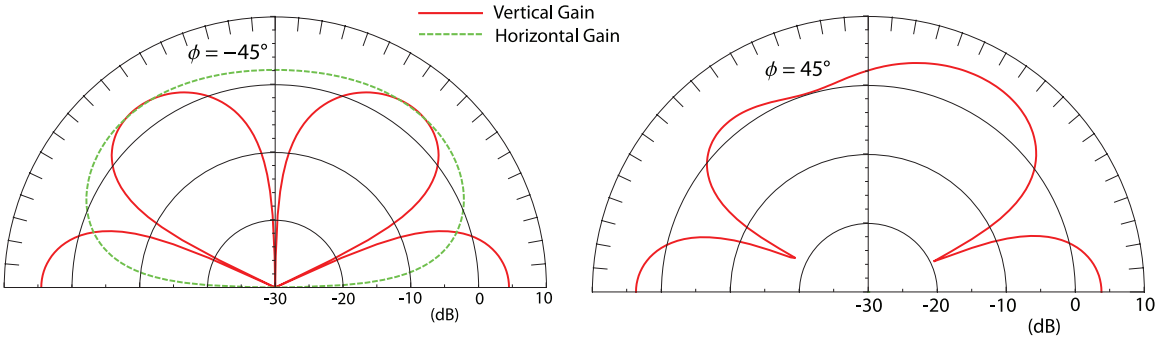

Fig. 3.1.14 Elevation patterns of vertical and horizontal gain in the $\phi = 45°$ and $-45°$ planes for the monopole at the center of the box at 1.192 GHz. The monopole is in the $\phi = 45°$ plane.

3.2 The Half-Loop on a Box

A model with a half-loop on the 10 cm box on an infinite ground plane is shown in Fig. 1. There are no measurements for this case, but the results can be compared for consistency. The current is shown in Fig. 1 for a voltage source at the center of the horizontal wire at 1 GHz, when the source location is near a current antinode. Color represents current magnitude over a two-decade log scale from red to violet and arrows show the imaginary part of current over three decades.

The input admittance with the voltage source at the center of the top wire is plotted in Fig. 2. The NEC–5 model was run with 3 and 6 segments on each vertical section of the loop to test convergence. The NEC–5 results show good convergence and a reasonable comparison with the admittance of the half-loop on an infinite ground plane. A NEC–4 model with 3 segments on the vertical sections also is in good agreement with other results. Fig. 3 and 4 show the result of increasing the number of segments on the vertical wires in the NEC–4 model. As with the monopole, a large capacitive reactance error is introduced with shorter segments at the junction in the NEC–4 model.

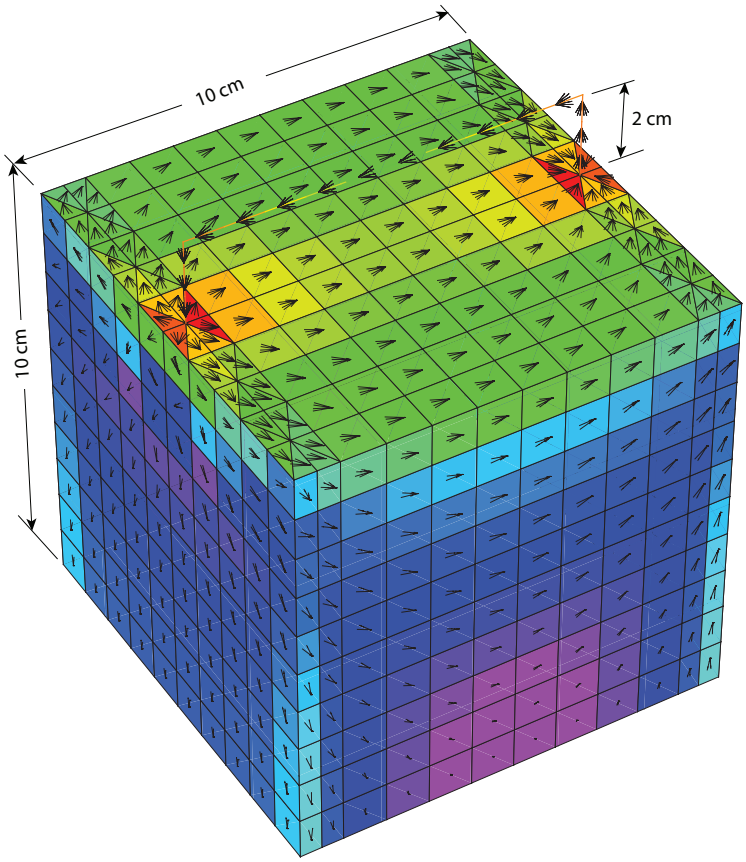

Fig. 3.2.1 Half-loop on a box. Loop height is 2 cm, length 9 cm and radius 0.9 mm. Currents are shown for a voltage source at the center of the top wire at 1 GHz.

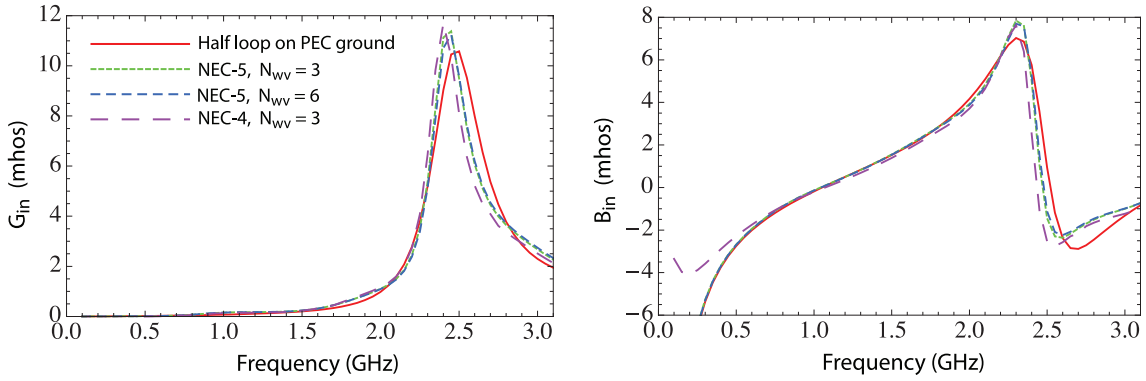

Fig. 3.2.2 Input admittance of the half-loop on a 10 cm box with voltage source at the center of the top wire. $N_{\rm wv}$ is the number of segments on the vertical sections of the half-loop.

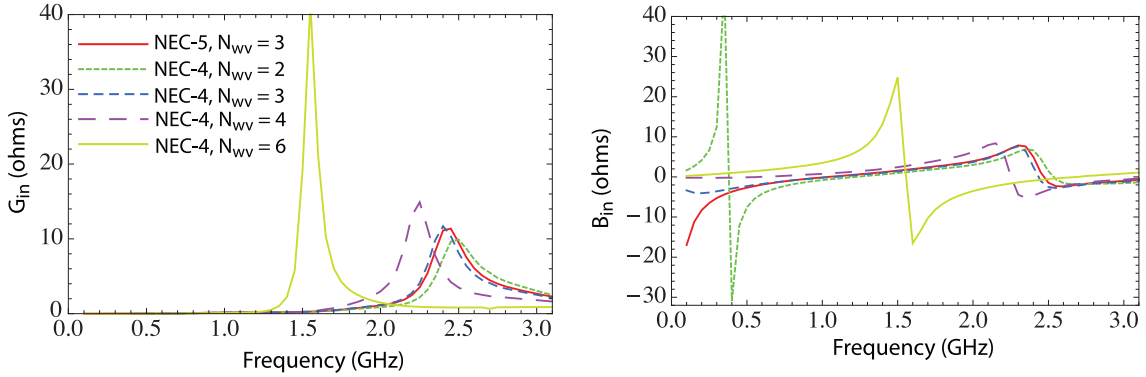

Fig. 3.2.3 Input admittance of the half-loop on a 10 cm box with voltage source at the center of the top wire, showing the error in the NEC–4 result as the number of vertical wire segments $N_{\rm wv}$ is increased.

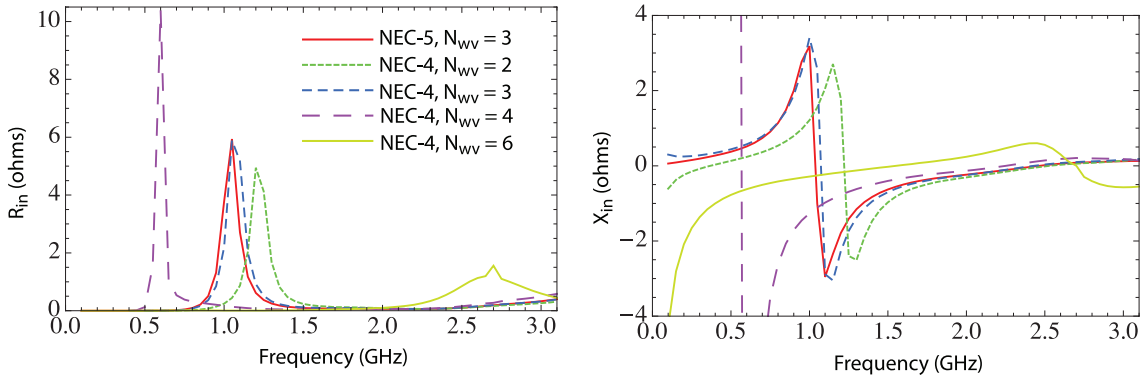

Fig. 3.2.4 Input impedance for the cases in Fig. 3.

Currents for the voltage source at the end of the half-loop at 200 MHz are shown in Fig. 5. At this lower frequency the current is nearly constant over the loop and is concentrated on the top surface of the box. Radiation patterns at 200 MHz are shown in Fig. 6. The maximum vertical gain is off the end of the loop and maximum horizontal gain is broadside above the ground plane. The power balance from integrating the radiated power was $P_{\rm rad}/P_{\rm in} = 1.0007$.

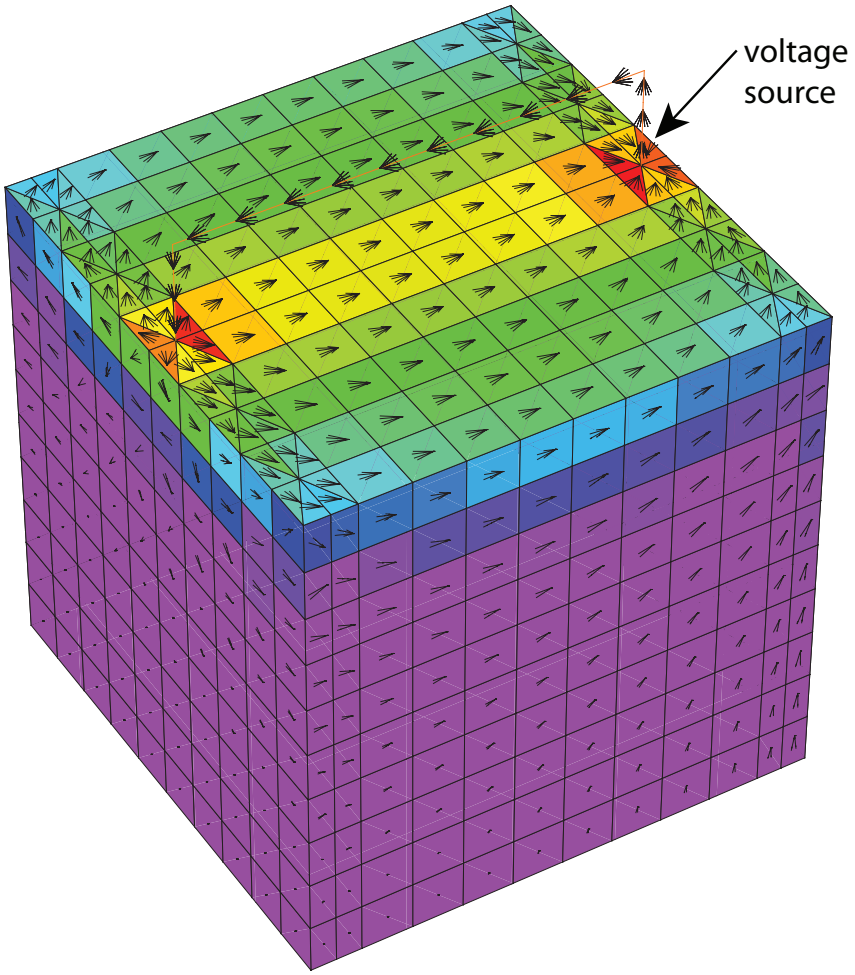

Fig. 3.2.5 Half-loop on a box showing currents with the voltage source at the base of the vertical wire at 200 MHz. Arrows show the imaginary part of current.

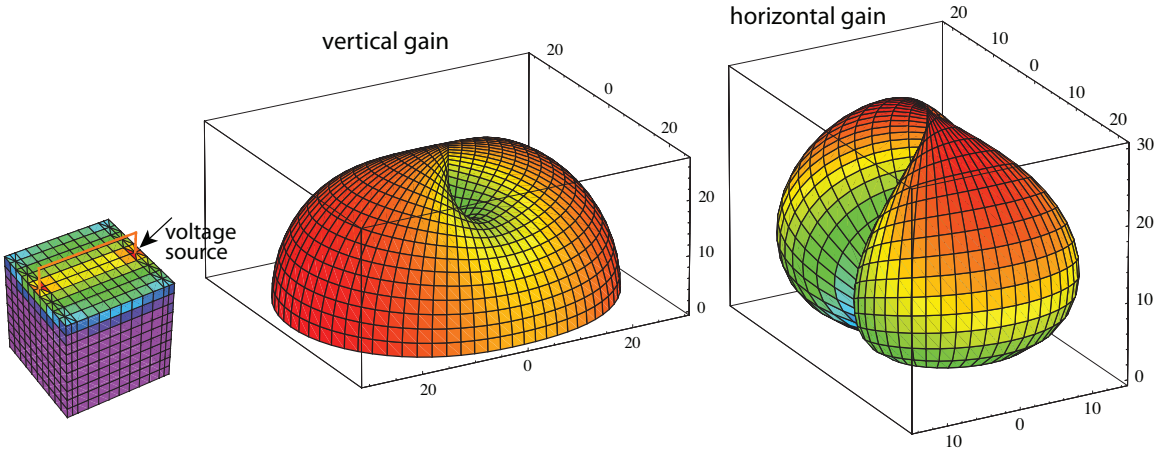

Fig. 3.2.6 Normalized gain patterns for the half-loop on the 10 cm box at 200 MHz with voltage source at the end. The maximum directive gains are 5.23 dB for vertical polarization (E_θ) and 2.20 dB for horizontal polarization (E_ϕ).

4. Antennas over Ground

The ground model in NEC-5 uses interpolation in tables of potentials for distances up to 3λ in ρ and about 1.5λ in height and asymptotic approximations at larger distances. NEC-4 also uses interpolation for E. The interpolation in NEC-5 should be more accurate than in NEC-4, and similar to the GN3 ground model in NEC-4.2. The NEC-4 and 5 ground models are sufficiently different that useful validation information can be obtained by comparing the two. Where possible other results have also been used for validation.

4.1 Horizontal Wires over Ground

A simple test for the ground model is a horizontal dipole lowered toward the interface. NEC-4 and 5 results for a dipole with length 0.4λ and radius $10^{-8}\lambda$ are shown in Fig. 1 for height h from 0.1λ to $10^{-7}\lambda$. The models had 15 segments for NEC-4 and 16 segments for NEC-5, so the voltage source was in the center in each model. Results are included for a NEC-5 strip model with 16 sections of triangular elements (32 elements) with strip width $4(10^{-8})\lambda$. Ground interaction tunes the dipole from capacitive to inductive over the height range. The three results are in good agreement over this range.

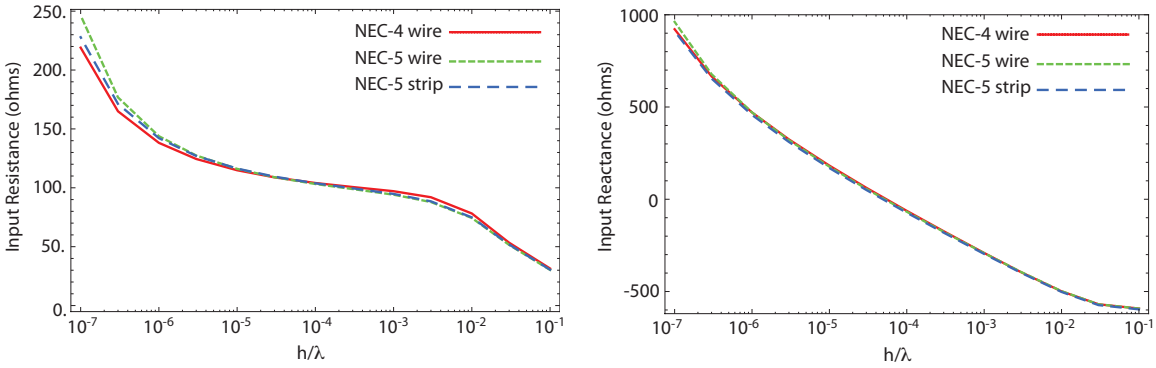

Fig. 4.1.1 Input impedance of a dipole with length 0.4λ and radius $10^{-8}\lambda$ for varying height h over dielectric ground with $\epsilon_r = 16$, comparing NEC-4, NEC-5 wire and NEC-5 triangular patch models.

On a long wire over ground the current driven by a voltage source has the form of an exponentially decaying mode, known as the transmission line mode or structure-attached mode and a slower decaying surface-attached mode [25]. The current magnitude on a 40λ wire is plotted in Fig. 2 from NEC-4 and NEC-5 for height h from 0.1λ to $10^{-4}\lambda$. The wire had a radius of $10^{-6}\lambda$ and was modeled with 1600 segments with a voltage source on segment 10, or on the inside end of segment 10 for NEC-5, and a matched load on the opposite wire end to reduce the standing wave from reflection. The transmission line mode dominates near the source, and the surface-attached mode becomes dominant for larger distances for heights of 0.01λ or less. While the two modes have comparable amplitudes an interference effect is seen. NEC-4 and 5 results are in good agreement over this range of heights and distances.

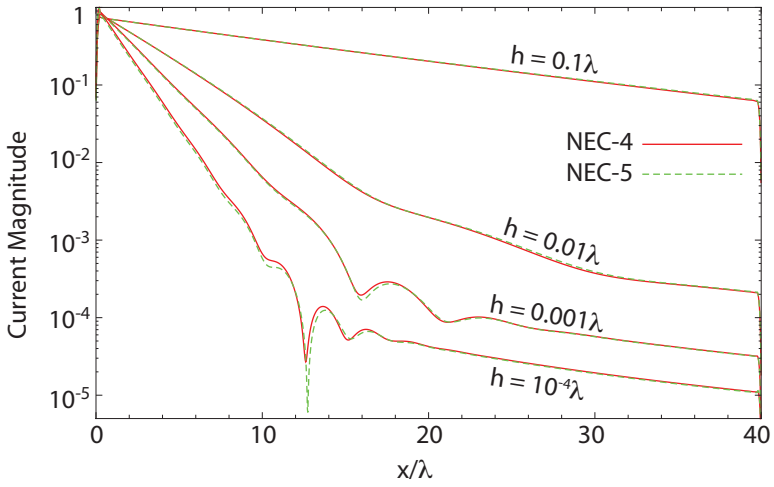

Fig. 4.1.2 Current on a 40λ wire at height h over ground with complex relative permittivity $\tilde{\epsilon}_r = 16 - j16$ ($\sigma = 0.00267$ S/m at 3 MHz) showing the exponential structure-attached modes and the slower decaying surface-attached modes.

An analytic result for the propagation constant of the transmission line mode can be obtained by solving for zeros of a modal equation in the complex plane [25]. To extract the phase and attenuation constants from the NEC solutions a 10λ wire with radius $10^{-6}\lambda$ and 400 segments was modeled over ground. The source was located on segment 4, or the inside end for NEC-5, for a position on the wire of about $x = 0.1\lambda$. A matched load at the opposite end of the wire was determined to minimize the standing wave so that the propagation constant could be determined accurately. The matched load can be determined numerically with one solution with NEC by saving the current $I(x)$. The current is reversed and added to the driven current as $I_m(x) = I(x) + V_L I(L - x)$ for wire length L. A measure of the standing wave is obtained as a mean-squared estimate of the second derivative of magnitude as $I_{SW} = \sum_i [-|I_m(x_{i-1})| + 2|I_m(x_i)| - |I_m(x_{i+1})|]^2$, summing over values of i away from the source and load regions, and this value is minimized by adjusting the complex V_L in a minimization routine. A result is shown in Fig. 3, showing the original current with standing wave and the current with matched load.

The current is assumed to propagate as $\exp(-ik_0\alpha x)$ where α is a normalized propagation constant. The normalized phase constant, $\mathrm{Re}[\alpha]$, and normalized attenuation constant, $\mathrm{Im}[\alpha]$, are found by linear regression on $\log[|I_m(x)|]$ and the phase of $I_m(x)$ after unwrapping the phase.

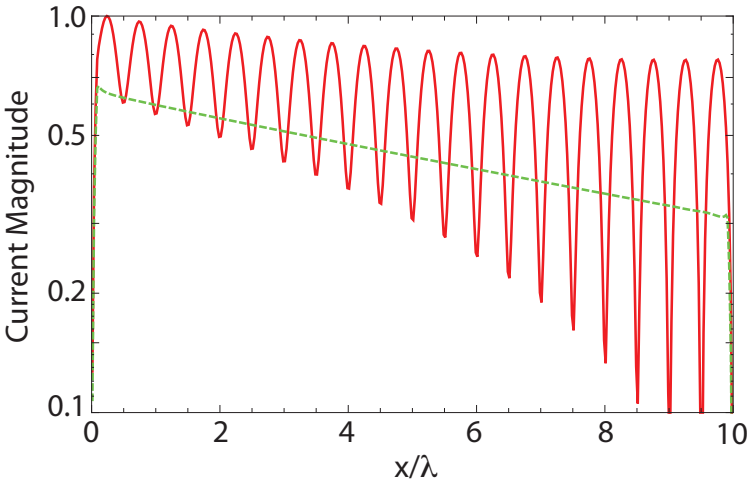

Fig. 4.1.3 Current on a 10λ wire with radius $10^{-6}\lambda$ at height $h = 0.1\lambda$ over ground with $\epsilon_r = 16$ showing the current with no termination (red) and with numerically matched termination (green).

The propagation constants determined in this way for NEC-4 and 5 models of wires and also NEC-5 strip models using triangular and rectangular patches are plotted in Fig. 4 and are in good agreement with the solution of the modal equation from [25]. There is increased difference for the strip models near the ground, but this may be a result of the model difference.

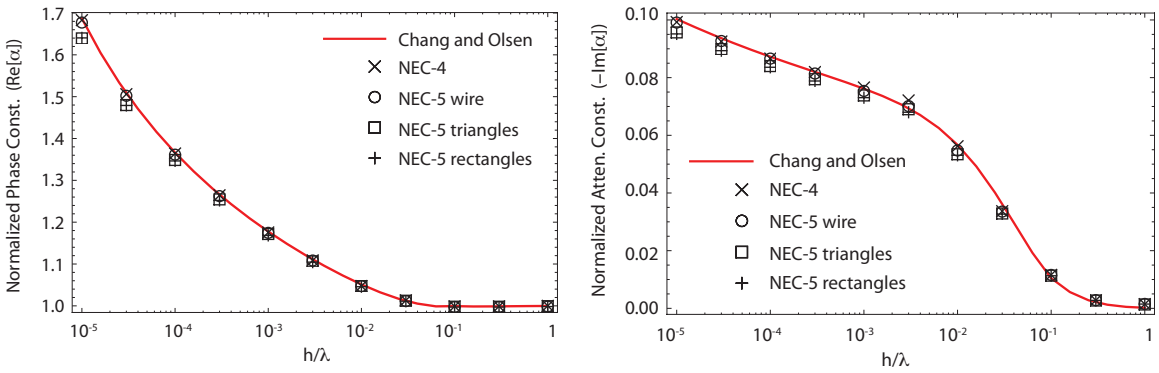

Fig. 4.1.4 Normalized propagation constant on a wire at height h over ground with $\epsilon_r = 16$ for the structure-attached mode $\exp(-jk_0\alpha x)$.

4.2 Loop Antennas over Ground

Modeling loop antennas over ground has always been problematic with NEC-4. Electrically small loops, at least in the vertical orientation, often give negative input resistance. This may result from the limited accuracy of the interpolated Sommerfeld integrals (about 3 to 4 places) and the treatment of scalar potential in the point-matched solution. Since the mixed-potential solution ensures that the approximated integral of scalar potential around the loop is zero, whether the potential is accurate or not, it might be expected to do better than NEC-4.

The first test is for an electrically small horizontal loop over ground. An analytic result for the impedance of a small horizontal loop with uniform current was developed by Wait [26]. For a small horizontal loop with radius a and wire radius c at height h_0 over ground Wait gets the input impedance as

$$Z_{in} = i\mu_0\omega a(P + S) \tag{1}$$

where

$$P = \pi \int_0^\infty [J_1(x)]^2 \exp(-B_0 x)\, dx \tag{2}$$

$$S = \pi \int_0^\infty [J_1(x)]^2 \frac{x - (x^2 + j2A^2)^{1/2}}{x + (x^2 + j2A^2)^{1/2}} \exp(-Bx)\, dx \tag{3}$$

with $J_1(x)$ the Bessel function, $A = a/\delta$ for skin depth $\delta = (2/\sigma\mu_0\omega)^{1/2}$, $B_0 = c/a$ and $B = (2h_0 + c)/a$. The term P represents the primary inductance of the loop and S is due to ground.

Wait [26] has the evaluation the integral for P as

$$P = \frac{2}{k_0}\left[\left(1 - \frac{k_0^2}{2}\right) K(k_0) - E(k_0)\right] \tag{4}$$

where $k_0 = 2(B_0^2 + 4)^{-1/2}$ and E and K are the elliptic integrals. However, Mathematica [19] evaluates the integral in (2) as

$$P = \frac{2 + B_0^2}{B_0} K(-4/B_0^2) - B_0 E(-4/B_0^2). \tag{5}$$

These results are not the same, and (5) agrees with the numerical integration of (2), so that value was used. It also agrees with numerical evaluation of the integral in Eq. (1) in [26]. The integral in Eq. (3) must be evaluated numerically. S does not include the radiation resistance of the loop, so the radiation resistance of a small loop, $R_{\rm rad} = 320\pi^6 a^4/\lambda^4$ was added.

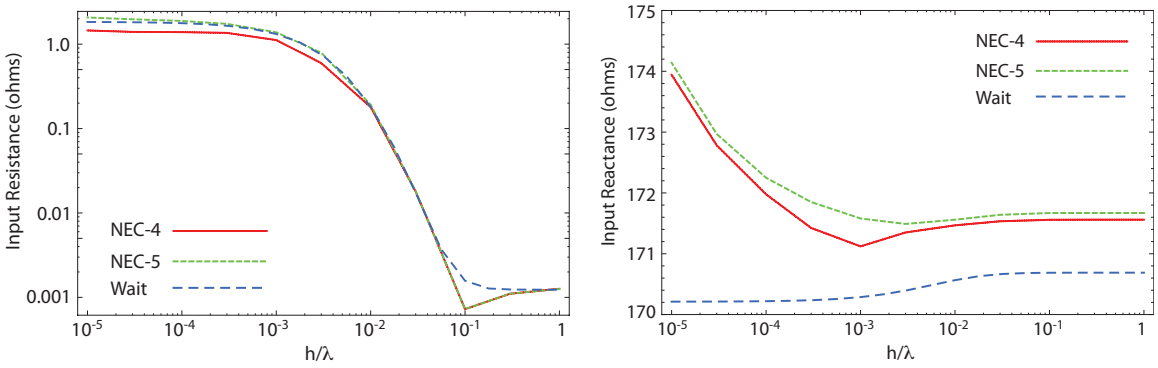

Fig. 4.2.1 Input impedance of a horizontal loop over ground comparing NEC–4, NEC–5 and Wait [26].

The input impedances from NEC-4 and 5 for a horizontal loop with $ka = 0.05$ and wire radius $10^{-6}\lambda$ at height h over ground with $\tilde{\epsilon}_r = 16 - j160$ ($\sigma = 0.0267$ S/m at 3 MHz) are plotted in Fig. 1 along with the solution from[26] using Eq. (5) for P. The agreement for resistance seems very good with NEC-5 the closest to the analytic solution. For reactance NEC-4 and 5 are in good agreement. The analytic solution does not get the trend for small h, but overall is within a percent. Using Eq. (4) from [26] for P the reactance goes from 177.2 ohms at $h/\lambda = 1$ to 176.7 ohms at $h/\lambda = 10^{-5}$, so that is not an improvement. A smaller loop might be better for the [26] solution, but possibly more difficult for NEC. May try that sometime.

The input impedances from NEC-4 and 5 for a vertical loop over ground are plotted in Fig. 2 versus ka. The thickness parameter of the loop was $\Omega = 2\log(2\pi a/c) = 15$ for loop radius a and wire radius c. The lower edge of the loop is at height h over the dielectric ground with $\epsilon_r = 16$. The results are in good agreement, with the typical downward shift in the resonant frequency for the mixed-potential solution with linear basis functions relative to NEC-4. The input resistances are plotted in Fig. 3 and 4 for small ka and h/a varying from 0.1 to 10. NEC-4 produces negative input resistance for small ka while NEC-5 results appear reasonable. The NEC-4 results are in reasonable agreement with NEC-5 for ka greater than about 0.16 or h/a of 10 or greater.

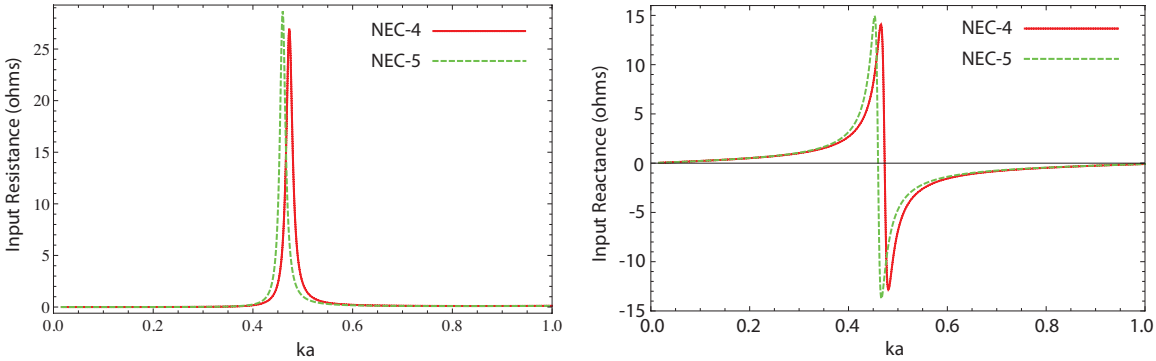

Fig. 4.2.2 Input impedance versus ks of a vertical loop over ground with thickness parameter $\Omega = 2\log(2\pi a/c) = 15$ for loop radius a and wire radius c. The lower edge of the loop is at $0.1a$ above the ground with $\epsilon_r = 16$.

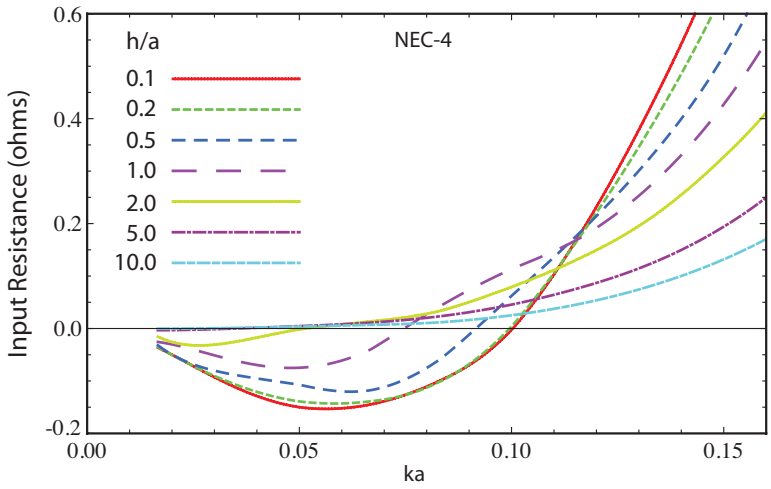

Fig. 4.2.3 Input resistance versus ka from NEC-4 for a small vertical loop over ground with loop radius a and wire radius c for thickness parameter $\Omega = 2\log(2\pi a/c) = 15$. Ground permittivity is $\epsilon_r = 16$ and height of the lower loop edge h/a is varied.

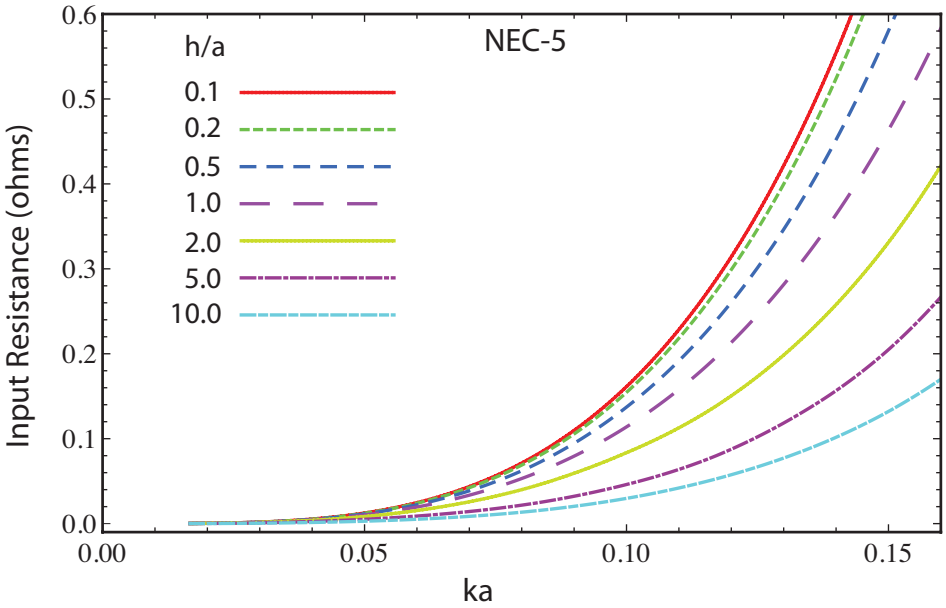

Fig. 4.2.4 Input resistance from NEC-5 for a small vertical loop over ground with loop radius a and wire radius c for thickness parameter $\Omega = 2\log(2\pi a/c) = 15$. Ground permittivity is $\epsilon_r = 16$ and height of the lower loop edge h/a is varied.

4.3 Monopole on a Radial-Wire Ground Screen

A monopole on a buried radial-wire screen can be modeled, as in NEC–4, with the base of the monopole at the ground plane and a segment sloping down from that point to the desired depth and then a horizontal wire to the required radius. Results are shown in Fig. 1 for a $\lambda/4$ monopole on a screen of 32 radials at a depth of $10^{-4}\lambda$ with wire radius $10^{-5}\lambda$. The ground had a complex relative permittivity of $15 - j15$. The radiation efficiency was determined by evaluating radiated field for θ from 0 to 90 degrees and ϕ at 0 and 5.63 degrees, halfway between radials, and computing average gain. The value for average gain assumes that radiation into the region not integrated repeats the pattern of the region integrated, where really there is no radiation into the lower half space, so the average gain value is divided by two to get radiation efficiency into the upper half space. NEC–4 and 5 are in close agreement except for very small screen radius, possibly because the differing representations of charge on the short screens have an effect. NEC–4 evaluated the Sommerfeld integrals for E while NEC–5 evaluated the integrals for potentials, so when they agree it is very likely the result is correct for the ideal ground screen model.

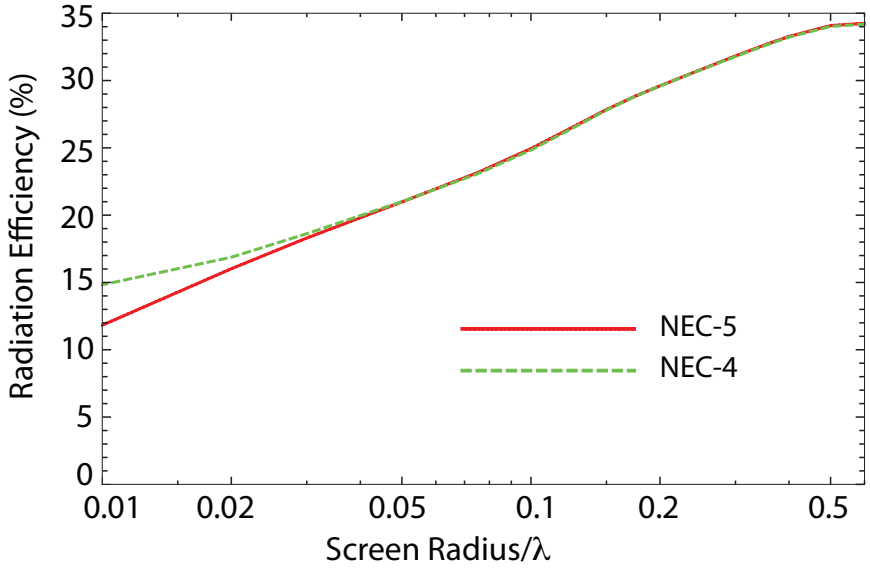

Fig. 4.3.1 Radiation efficiency of a $\lambda/4$ monopole on a screen of 32 radial wires with varying screen radius.

In entering the model the sloping segment and horizontal radial are entered first and rotated for 32 radials with a GR 0, 32 command, then the monopole is entered so that NEC–5 can take advantage of the partial symmetry. With 32 radials and 23 segments on each radial the time for NEC–5 to fill the matrix was 14 times faster than NEC–4.

A source of uncertainty in modeling antennas with ground is the ground parameters permittivity and conductivity. Often ground parameters are not measured, but average values for the ground type are assumed. Plots are included in Appendix B in an attempt to show the sensitivity to ground parameters for a monopole on a radial-wire screen. The antenna is seen to become less sensitive to ground parameters as the number of radials is increased.

5. Conclusion

Many of the results here were chosen to illustrate known limitations of NEC–4, and NEC-5 is seen to be more accurate for most situations. One case where NEC–4 beats NEC–5 is in convergence for a dipole, since NEC–5 uses linear, triangular basis functions while NEC–4 has a higher order sinusoidal basis. The mixed-potential code should converge faster with a higher-order basis, but there are no plans to add that to NEC–5. So NEC–4 may remain the preferable code for modeling antennas such as Yagis where accurate resonant frequencies are critical.

In cases where NEC–4 and 5 agree we can have considerable confidence in the accuracy of the results. This is particularly valuable for antennas with ground, where it is difficult to find independent results, and measurements usually involve uncertainties in physical modeling errors, such as ground parameters and the contact of wires and surfaces with the ground. When NEC–4 and 5 agree it seems very likely that the results are correct for the idealized model, since NEC–4 is evaluating electric field while NEC–5 is evaluating potentials and different methods are used to enforce the boundary conditions. In cases such as a small loop over ground it is obvious that NEC–4 fails.

Results in this manual were generated in debugging and validating NEC–5. Other comparisons may be added in the future as they are developed or if contributed or suggested by users.

References

[1] G. J. Burke and A. J. Poggio, *Numerical Electromagnetics Code (NEC) – Method of Moments*, UCID-18834, Lawrence Livermore National Laboratory, CA, January 1981.

[2] G. J. Burke and A. J. Poggio, *Numerical Electromagnetics Code (NEC–4) – Method of Moments*, UCRL-MA-109338, Lawrence Livermore National Laboratory, CA, January 1981.

[3] G. J. Burke, A. J. Poggio, *Numerical Electromagnetics Code NEC–5 – Method of Moments, User's Manual*, LLNL-SM-742937, Lawrence Livermore National Laboratory, CA, November 22, 2017.

[4] S. M. Rao, D. R. Wilton, A. W. Glisson, "Electromagnetic Scattering by Surfaces of Arbitrary Shape," *IEEE Trans. Antennas and Propagation*, Vol. AP-30, No. 3, pp. 409-418, May 1982.

[5] W. A. Johnson, D. R. Wilton, R. M. Sharpe, *Patch Code Users' Manual*, Report SAND87-2991, Sandia National Laboratories, Albuquerque NM, May 1988.

[6] S. U. Hwu and D. R. Wilton, *Electromagnetic Scattering and Radiation by Arbitrary Configurations of Conducting Bodies and Wires*, Tech. Rept. 87-17, University of Houston, May 23, 1988.

[7] D. R. Wilton, S. U. Hwu, *Junction Code User's Manual*, Report 87-18, University of Houston, May 30, 1989.

[8] S. M. Rao, "Electromagnetic Scattering and Radiation of Arbitrary Shape Surfaces by Triangular Patch Modeling," Ph.D. dissertation, University of Mississippi, Aug. 1980.

[9] M. F. Costa and R. F. Harrington, "Minimization of Radiation from Computer Systems," International Elecrical Electronics Conference and Exposition Proceedings, Toronto, Canada, pp. 660-665, Sept. 1983.

[10] M. F. Costa and R. F. Harrington, "Electromagnetic Radiation and Scattering from a System of Conducting Bodies Interconnected by Wires," Report TR-83-8, Syracuse University, April 1983.

[11] R. M. Sharpe, J. B. Grant, N. J. Champagne, W. A. Johnson, R. E. Jorgenson, D. R. Wilton, W. J. Brown, J. W. Rockway, "EIGER: Electromagnetic Interactions GEneRalized", IEEE Antennas and Propagation Society International Symposium Proceedings, 1997, Montreal, Quebec, Canada, 13-18 July 1997.

[12] K. A. Michalski, D. Zheng,"Electromagnetic Scattering and Radiation by Surfaces of Arbitrary Shape in Layered Media, Part I: Theory", *IEEE Trans. Antennas and Propagation*, Vol. AP-38, No. 3, pp. 335-344, March 1990.

[13] K. A. Michalski, D. Zheng,"Electromagnetic Scattering and Radiation by Surfaces of Arbitrary Shape in Layered Media, Part II: Implementation and Results for Contiguous Half-Spaces", *IEEE Trans. Antennas and Propagation*, Vol. AP-38, No. 3, pp. 345-352, March 1990.

[14] G. J. Burke, *NEC5GI Graphical Interface for NEC–5*, LLNL-SM-747061, Lawrence Livermore National Labotratory, CA, March 1, 2018.

[15] D. H. Werner, "An Exact Formulation for the Vector Potential of a Cylindrical Antenna with Uniformly Distributed Current and Arbitrary Radius," *IEEE Trans. Antennas and Propagation*, Vol. 41, No. 8, pp. 1009-1018, Aug. 1993.

[16] D. H. Werner, "A Method of Moments Approach for the Efficient and Accurate Modeling of Moderately Thick Cylindrical Wire Antennas," *IEEE Trans. Antennas and Propagation*, Vol. 46, No. 3, pp. 373-381, March 1998.

[17] P. C. Waterman, "Matrix Formulation of Electromagnetic Scattering," *Proceedings of the IEEE*, Vol. 53, pp. 805-812, August 1965.

[18] B. D. Popović, M. B. Dragović and A. R. Djordjević, *Analysis and Synthesis of Wire Antennas*, Research Studies Press, New York, 1982.

[19] Wolfram Research, Inc., *Mathematica*, V. 10, Champaign, IL, 2014.

[20] R. W. P. King, *The Theory of Linear Antennas*, Harvard Univ. Press, Cambridge, MA, 1956.

[21] G. J. Burke, *Treatment of Small Wire Loops in the Method of Moments Code NEC*, UCID-21196, Lawrence Livermore National Laboratory, CA, October, 1987.

[23] S. Bhattacharya, S. A. Long and D. R. Wilton, "The Input Impedance of a Monopole Antenna Mounted on a Cubical Conducting Box," *IEEE Trans. Antennas and Propagation*, Vol. 35, No. 7, pp. 756-762, July 1987.

[24] A. W. C. Chu, S. A. Long and D. R. Wilton, "The Radiation Pattern of a Monopole Antenna Attached to a Conducting Box," *IEEE Trans. Antennas and Propagation*, Vol. 38, No. 12, pp. 1907-1912, Dec. 1990.

[25] D. C. Chang and R. G. Olsen, "Excitation of an Infinite Antenna Above a Dissipative Earth," *Radio Science*, Vol. 10, No. 8, 9, pp. 823-831, Aug.-Sept. 1975.

[26] J. R. Wait and K. P. Spies, "Low-Frequency Impedance of a Circular Loop over a Conducting Ground," *Electronics Letters*, Vol. 9, No. 15, pp. 346-348, July. 1973.

Appendix A

A.1 Accuracy of Kernel Evaluation

Errors in evaluating a potential integral on a wire segment using the extended kernel and the reduced kernel relative to the exact kernel are shown in Fig. 3.1.1. This appendix includes plots of the errors as ρ and z are increased away from the source segment

For the self-term, Fig. 1, the error in the extended kernel is seen to be nearly independent of Δ and to increase with increasing radius a due to the approximate evaluation of the first integral in (3) containing the phase information. The error in the reduced kernel depends on the thickness ratio, and is poor when Δ/a is on the order of 1 or less. Similar plots are shown in Fig. 2 through 4 for ρ equal to 3, 10 and 100 times a. With increasing ρ the extended kernel accuracy remains limited by the phase error. For the reduced kernel the error related to Δ/a decreases with increasing ρ, and the phase error becomes the limiting factor at large a/λ.

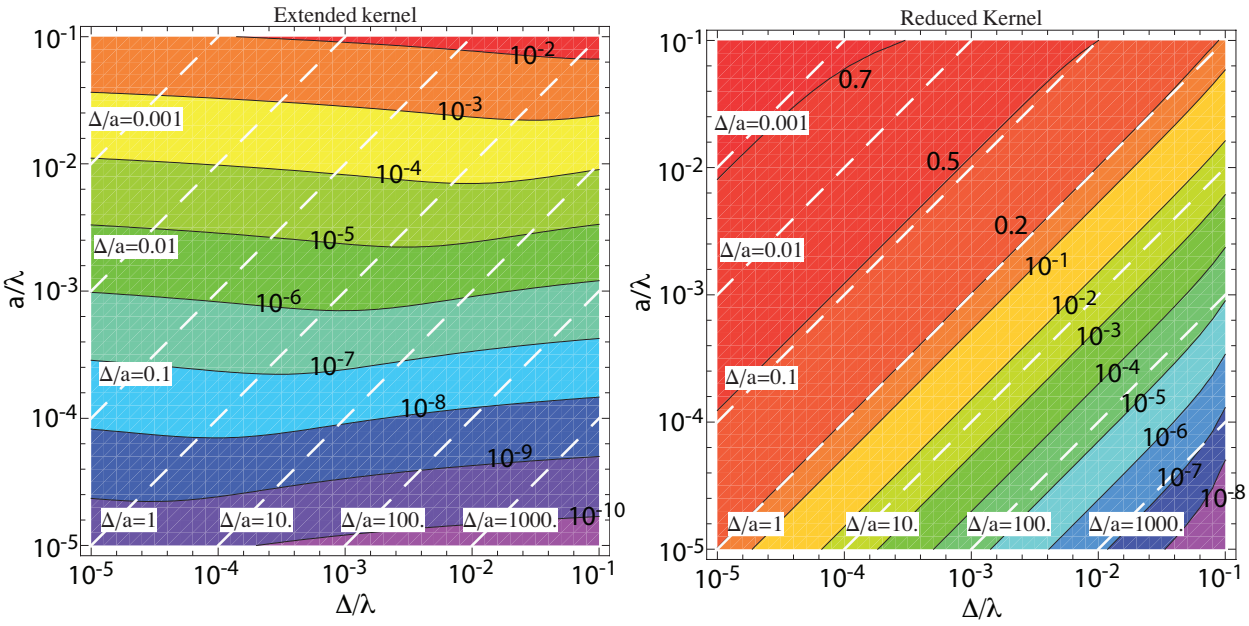

Fig. A.1 Errors in the extended and reduced kernels relative to the exact kernel for the evaluation point at the center of the segment (self-term) with $\rho = a$ for the extended kernel, $\rho = 0$ for the reduced kernel.

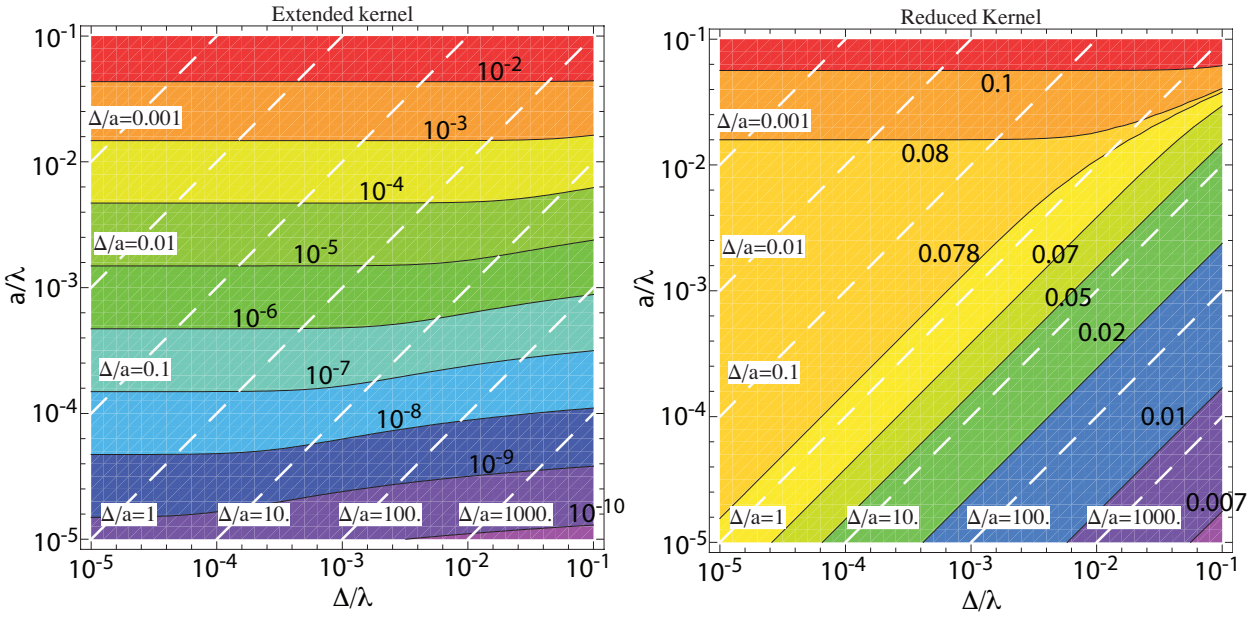

Fig. A.2 Errors in the extended and reduced kernels at $\rho = 3a$ and $z = 0$.

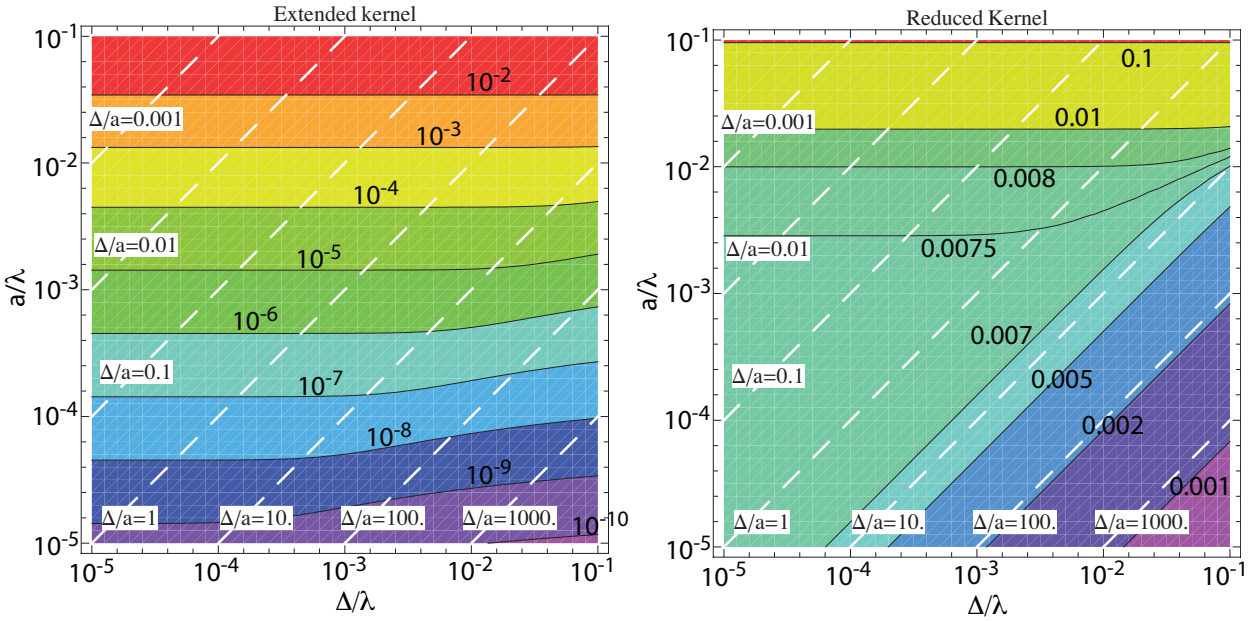

Fig. A.3 Errors in the extended and reduced kernels at $\rho = 10a$ and $z = 0$.

Errors with increasing z are shown in Fig. 5 through 7. For these plots ρ was equal to a for both extended and reduced kernels. In the reduced kernel solution the evaluation point would be on the axis, but putting it on the surface gave a smaller error and is the way that it is used in evaluating the first integral in (3). Again, the extended kernel is limited only by the phase error which decreases with increasing z. For the reduced kernel both the error related to Δ/a and the phase error decrease with increasing z.

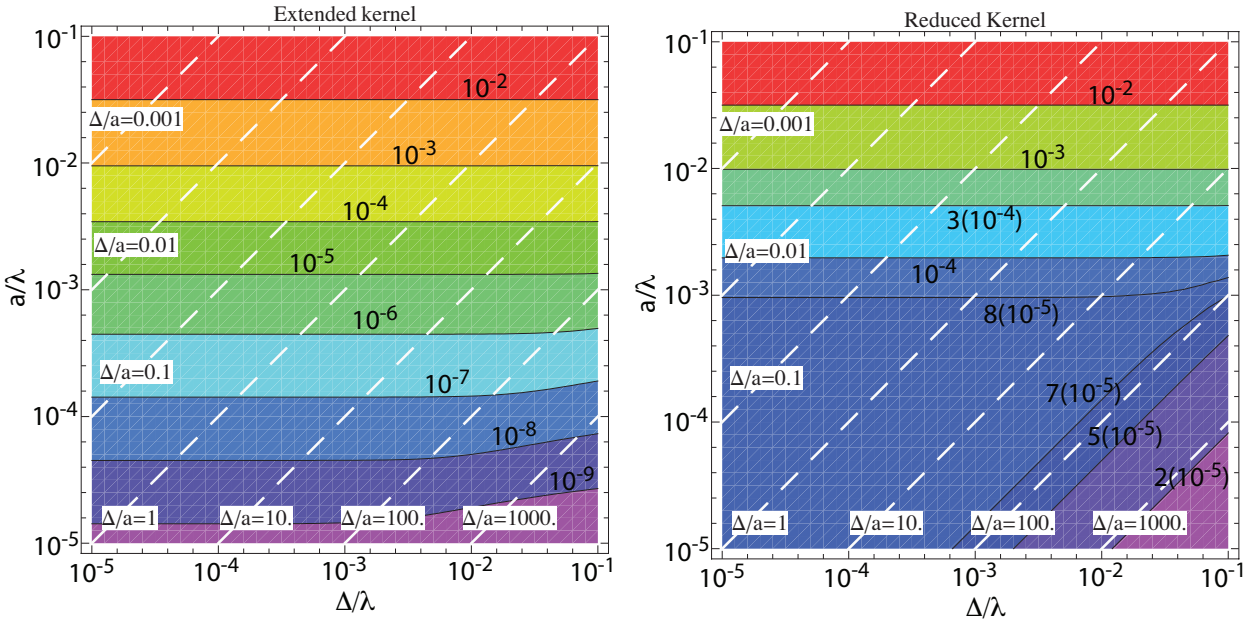

Fig. A.4 Errors in the extended and reduced kernels at $\rho = 100a$ and $z = 0$.

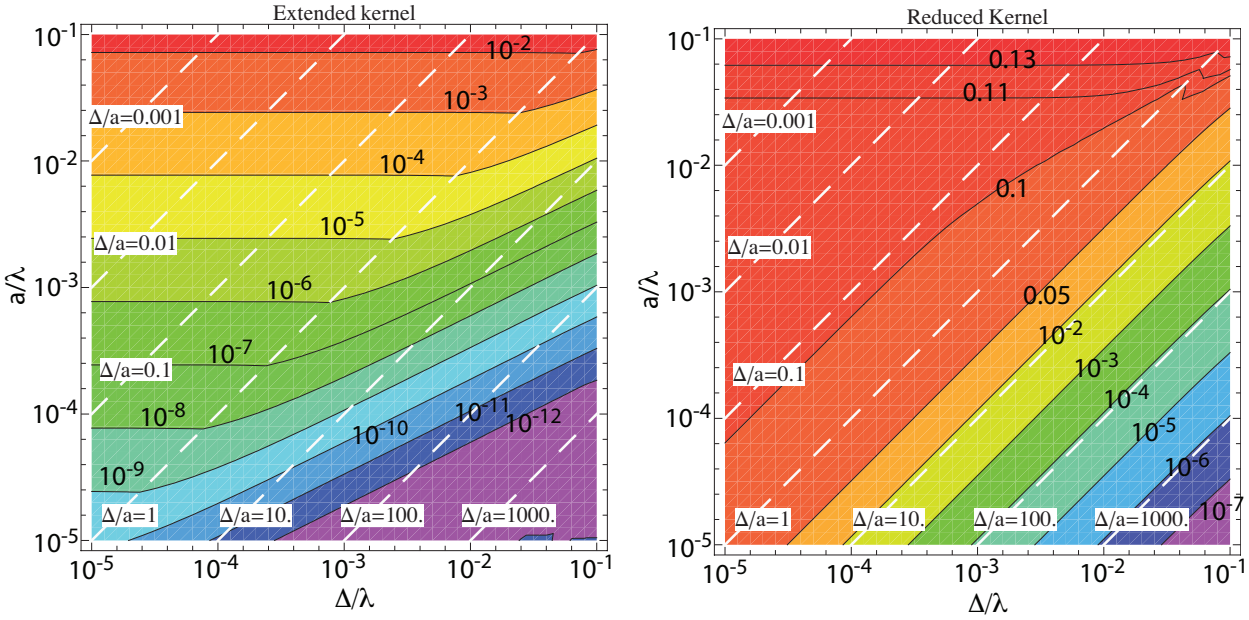

Fig. A.5 Errors in the extended and reduced kernels at $\rho = a$ and $z = \mathrm{Max}(\Delta, a)$.

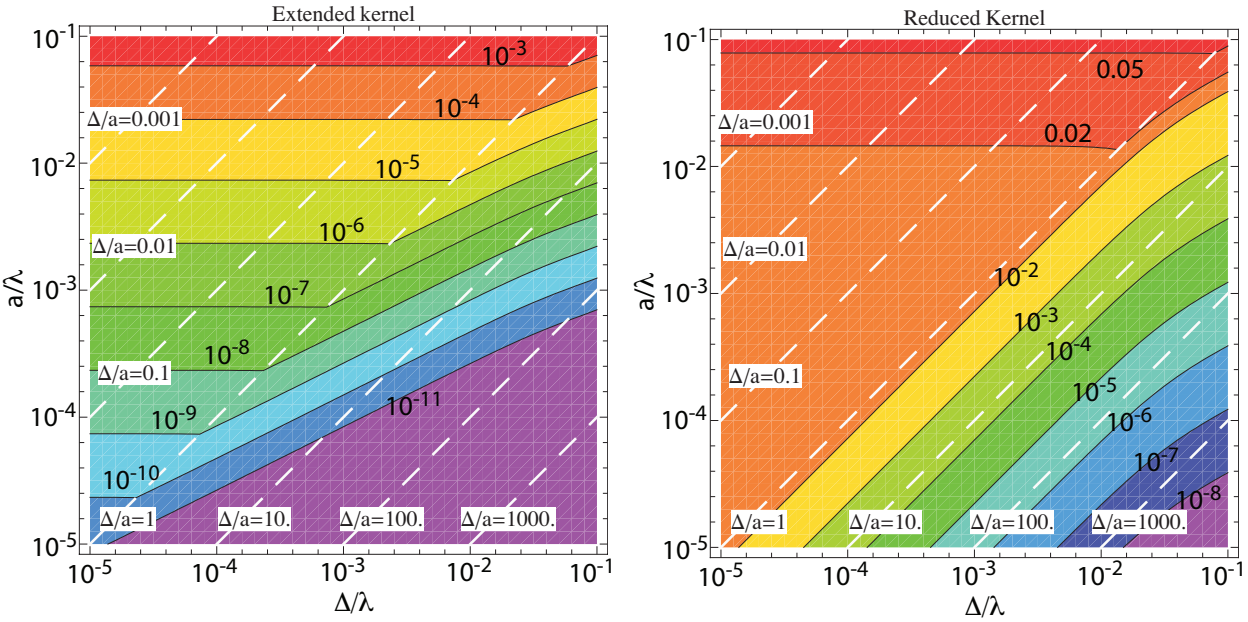

Fig. A.6 Errors in the extended and reduced kernels at $\rho = a$ and $z = 5 \times \mathrm{Max}(\Delta, a)$.

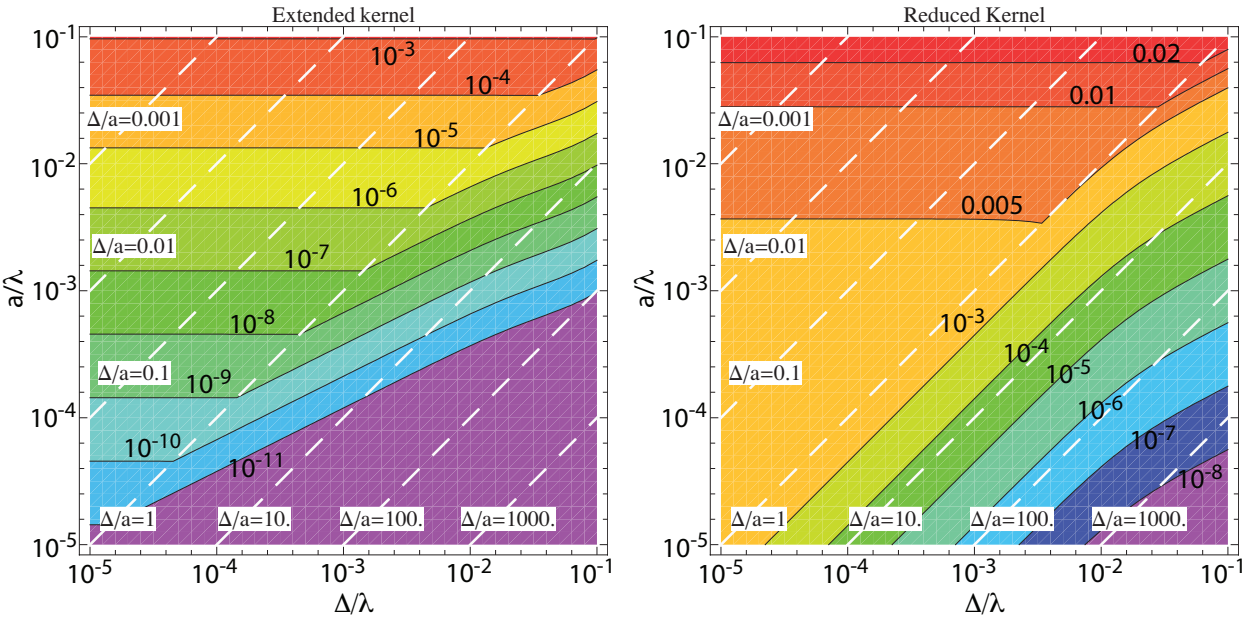

Fig. A.7 Errors in the extended and reduced kernels at $\rho = a$ and $z = 10 \times \mathrm{Max}(\Delta, a)$.

Appendix B

B. Effect of Ground Parameters for a Monopole on a Radial-Wire Screen

Sources of uncertainty in modeling antennas that involve ground are the ground parameters and condition of the ground. Often ground permittivity and conductivity are not measured and just average values for the ground type are assumed. Plots in this appendix demonstrate the sensitivity of a monopole on a radial-wire ground screen to ground permittivity and conductivity for ground screens with 8, 16, 32 nd 128 radials.

The optimum efficiency of a radial-wire ground screen near a quarter wave in radius occurs when the screen radius is about a quarter wave in electrical length in the ground. Since this length would depend on the ground parameters and proximity of the wires to the ground surface, the free-space wavelength is used for these plots, with the screen radius $\lambda_9/4$, somewhat longer than optimum, and monopole height also $\lambda_9/4$. The screens are buried at $10^{-4}\lambda_0$ in the ground and all wire radii are $10^{-5}\lambda_0$.

Other conditions affecting an antenna in ground include ground parameters varying with depth, irregular ground surface and contact conditions and chemical reactions between the wires and the ground. These are factors for real antennas rather than the ideal antennas modeled with NEC and are not considered here.

Fig. B.1 shows radiation efficiencies of a monopole on a radial-wire ground screen for varying ground parameters, relative permittivity and conductivity, Scales are shown for both conductivity at 1 MHz and the imaginary part of the complex relative permittivity $\tilde{\epsilon}_r = \epsilon_r - j\sigma/(\omega\epsilon_0)$. Some people find these efficiencies to be surprisingly low. Much of the power may enter the ground beyond the radius of the ground screen, so only higher ground conductivity can increase efficiency.

Fig. B.2 and B.3 show the input resistance and reactance of the antennas for varying ground permittivity and conductivity. As expected, more radials in the screen reduces the variation of antenna impedance with ground parameters. The color scale in these plots remains constant between antennas but the contour lines change.

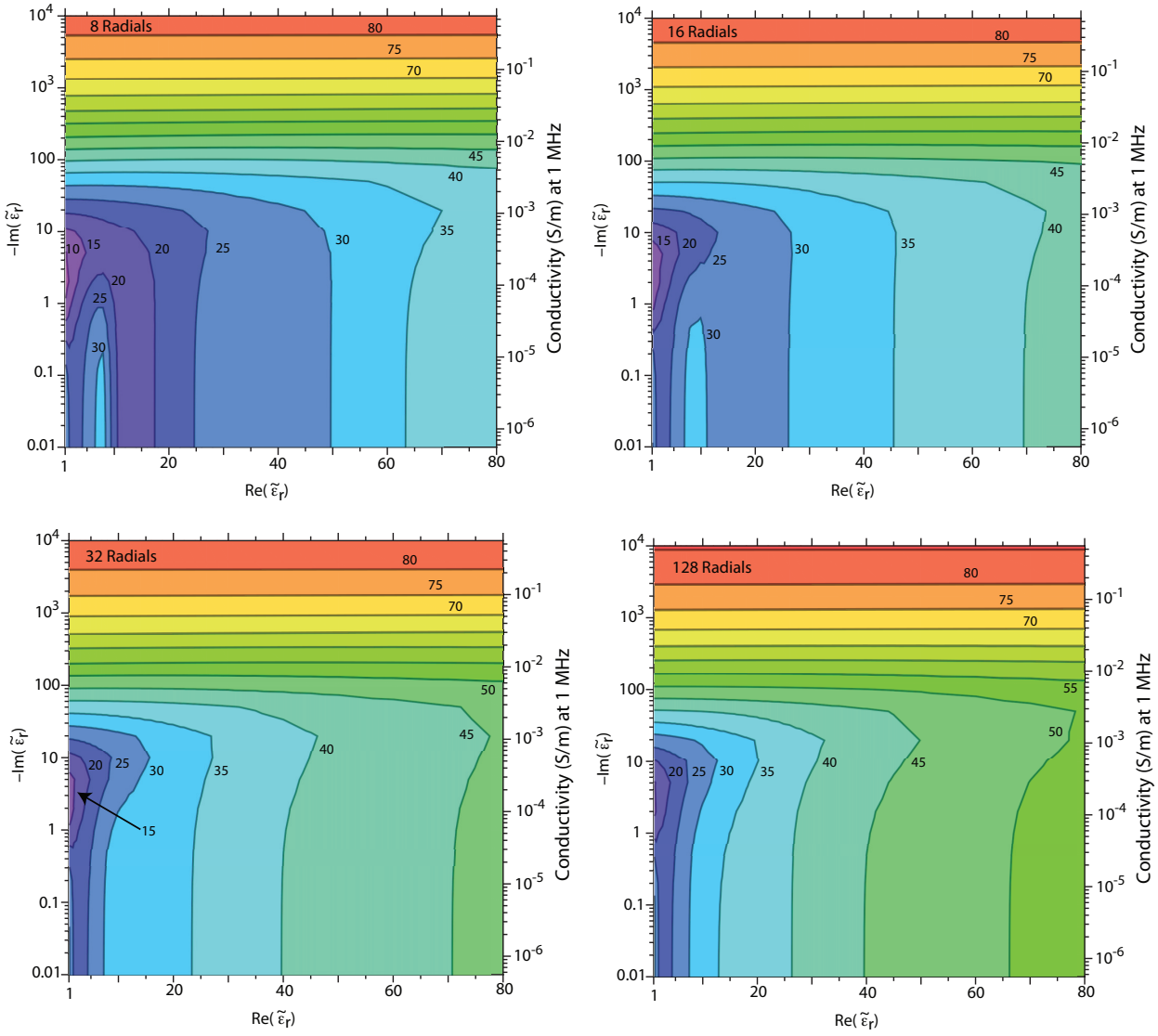

Fig. B.1 Radiation efficiency in percent for a $\lambda/4$ monopole on a radial wire ground screen for varying complex relative permittivity $\tilde{\epsilon}_r = \epsilon_r - j\sigma/(\omega\epsilon_0)$

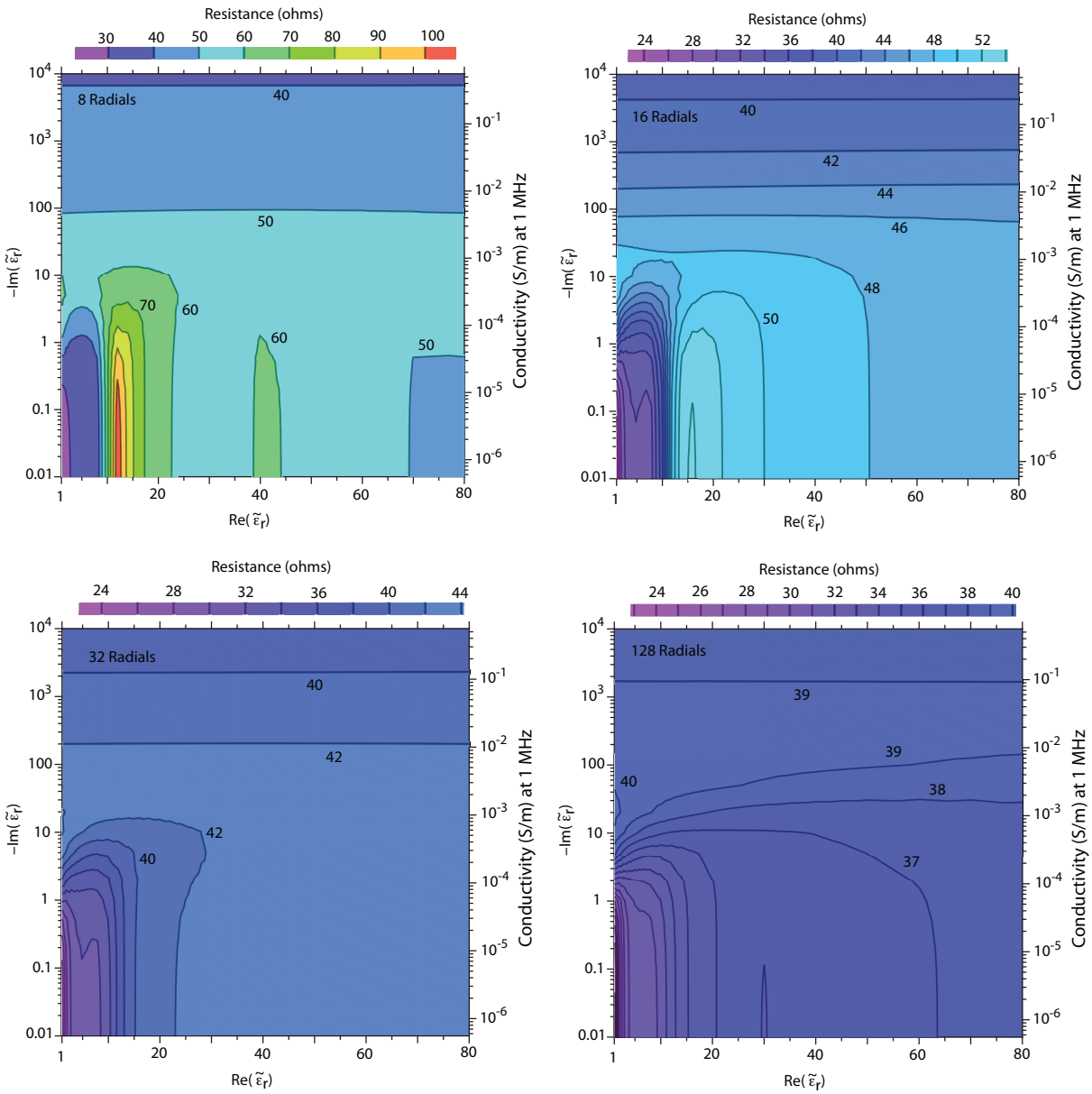

Fig. B.2 Input resistance for a $\lambda/4$ monopole on a radial wire ground screen for varying complex relative permittivity $\tilde{\epsilon}_r = \epsilon_r - j\sigma/(\omega\epsilon_0)$

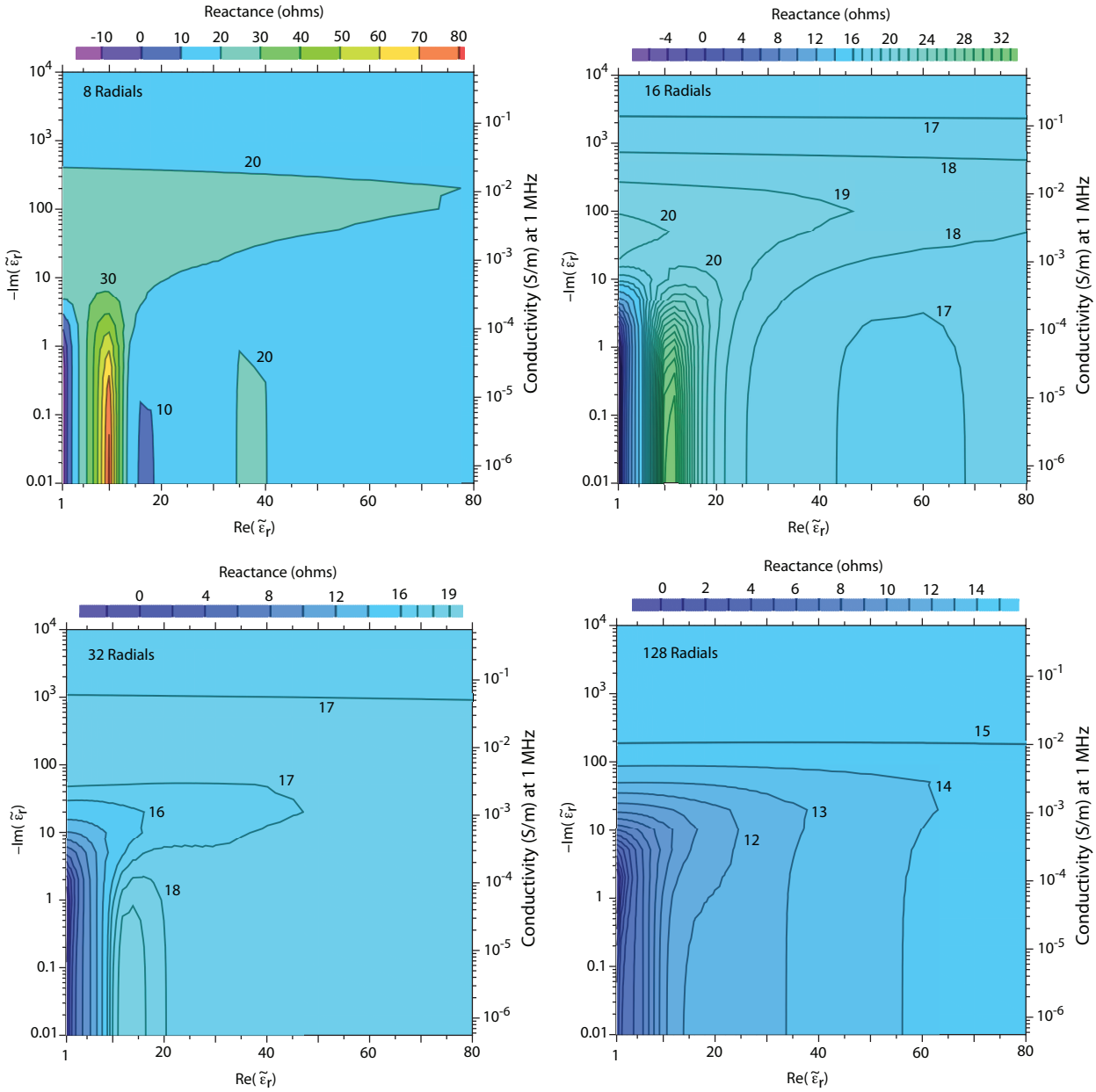

Fig. B.3 Input reactance for a $\lambda/4$ monopole on a radial wire ground screen for varying complex relative permittivity $\tilde{\epsilon}_r = \epsilon_r - j\sigma/(\omega\epsilon_0)$